Spring 4-21-2017

Design of 3D Macroporous Inverse Opal TiO2 Binary and Ternary Composites Sensitized with Gold Nanoparticles and CdS Quantum Dots for Photocatalysis

Daniel A. Corella
Kennesaw State University

Design of 3D Macroporous Inverse Opal TiO_2 Binary and Ternary Composites Sensitized with Gold Nanoparticles and CdS Quantum Dots for Photocatalysis

by

Daniel A. Corella

B.S. Chemistry

Kennesaw State University, 2014

Submitted in Partial Fulfillment of the Requirements

For the Degree of Master of Science in the

Department of Chemistry and Biochemistry

Kennesaw State University

May 2017

---	---
Committee Chair	Graduate Program Coordinator
---	---
Committee Member	Department Chair
---	---
Committee Member	College Dean

ACKNOWLEDGMENTS

Dr. Bharat Baruah for all the support and guidance

William A. Mendez Gil and all the members of the Baruah group for their insights and for bringing some much-needed energy to the quiet lab

Kennesaw State University's Department of Chemistry and Biochemistry for providing me with this opportunity

Mom and Dad for being there when things got tough

ABSTRACT

Materials composed of titanium (IV) oxide (TiO_2) have received enormous scientific interest due to titania's abundance, non-toxicity, and photocatalytic proficiency, however its large band gap limits its applicability under ambient conditions. Various attempts have been made to incorporate titania into composite systems to sensitize it for activity under a broader range of wavelengths. One such method includes utilizing narrow band gap semiconductors to form an electron transfer process analogous to photosynthesis referred to as a Z-scheme. Z-scheme systems can catalyze the decomposition of aqueous pollutants via generation of reactive oxygen species after input of sunlight. This work reports the design of a photocatalyst consisting of macroporous inverse opal (*io*) TiO_2 embedded with gold nanoparticles (AuNPs) and cadmium sulfide quantum dots (CdS QDs) into binary and ternary systems. These composites, labeled *io*TiO_2-Au, *io*TiO_2-CdS, and *io*TiO_2-Au-CdS are characterized via SEM, EDX, solid-state UV-vis, and Raman, and are subsequently evaluated for their photocatalytic efficiency against the pollutant analog trypan blue (TryB) under UV and white light LED lighting conditions. It was found that binary *io*TiO_2-CdS exhibits the best photocatalytic performance, with a rate constant 7.8, 5.2, 6.5, and 1.6 times faster than singular *io*TiO_2 and CdS, binary *io*TiO_2-Au, and ternary *io*TiO_2-Au-CdS under UV, respectively. Under white light LED all systems exhibit reduced activity, with *io*TiO_2-Au-CdS and *io*TiO_2-CdS showing no statistical difference, however, the ternary system performed most consistently across both light sources, retaining 92% of its UV performance. Loss of CdS due to photocorrosion limits recyclability of the thin films.

TABLE OF CONTENTS

LIST OF TABLES/LIST OF FIGURES

LIST OF KEY ACRONYMS

AIBA: 2,2′-Azobis(2-methylpropionamidine) dihydrochloride

AOP: Advanced oxidation process

EDX: Energy dispersive X-ray analysis

io: Inverse opal

LED: Light emitting diode

LSPR or SPR: (Localized) surface plasmon resonance

nc: nanocrystalline

NP(s): Nanoparticle(s)

PBG: Photonic band gap

PC: Photonic crystal

PMMA: Poly(methyl methacrylate)

PS: Polystyrene

PVP: Polyvinylpyrrolidone

SEM: Scanning electron microscopy

SILAR: Successive ionic layer absorption and reaction

SPD: Spectral power distribution

TryB: Trypan Blue

TiBALDH: titanium(IV)-bis(ammonium lactate) dihydroxide

QD(s): Quantum dot(s)

CHAPTER 1. INTRODUCTION

1.1 TiO_2: A Versatile Heterogeneous Photocatalyst

Water pollution generated by runoff from agricultural and industrial sources poses major health risks to civilization, which makes developing effective methods for treating contaminated sources of paramount interest to the scientific community. One prospect that has seen significant attention in recent years is the utilization of light sensitive semiconductors to photocatalytically facilitate the degradation of pollutants into biologically innocuous substances. Titanium (IV) oxide, also known as titania, is one such photocatalyst that is renowned for being cheap, chemically stable, and non-toxic.[1-3] After the discovery of the Honda-Fujishima effect in 1972, wherein TiO_2 utilizes light to split water into H_2 and O_2,[4] titania has been utilized for a wide variety of applications ranging from dye-sensitized solar cells,[5] to anti-fogging coatings on glass[6,7] to degradation of herbicides, dyes, and other industrial chemical waste products.[8,9] Titania occurs in three polymorphs; anatase, rutile, and brookite (Figure 1.1),[10-12] of which the first two have been studied more extensively for most applications.[13]

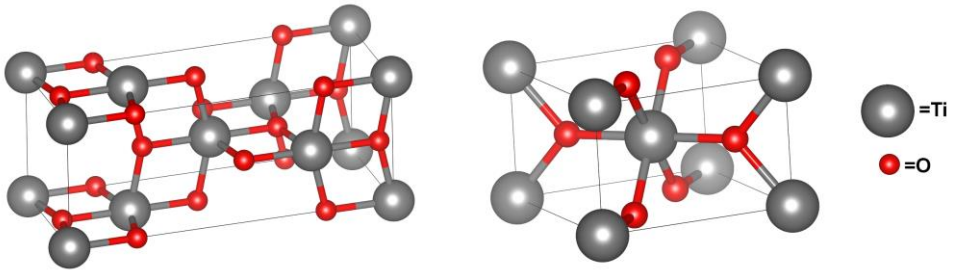

FIGURE 1.1 TiO_2 polymorph crystal structures for anatase (left) and rutile (right). Brookite not featured. Images made using VESTA 3 3D visualization software.[10-12]

In the pure phase, it is generally accepted that anatase is more active than rutile for photocatalysis.[14,15] Luttrell et al. compared the photocatalytic activity of methyl orange degradation for anatase and rutile thin films and found anatase to be roughly twice as active as rutile.[15] Liu et al. utilized *in situ* diffuse reflectance infrared Fourier transform (DRIFTS) to investigate photocatalytic CO_2 reduction and found that unpretreated anatase demonstrated better CO and CH_4 production than brookite and rutile.[13] Cappelletti et al. compared titania polymorph composites for photoreduction of Cr(VI) and found anatase-brookite and anatase-rutile P25 had 15% higher activity than pure rutile samples, which the authors attribute to intrinsic features to rutile such as improved light absorption and exposed faces.[16]

Despite its versatility, a major hindrance to titania's usefulness is that it possesses a relatively large electronic band gap of ≈ 3.2 eV which necessitates that incident light have a wavelength of 387 nm or less for excitation to occur.[17] UV radiation makes up roughly 5% of sunlight, with much of the high-energy UV rays like UVB (280 - 315 nm) and UVC (100 - 280 nm) being partially or completely filtered out by the ozone layer.[18-20] Thus, to maximize efficiency under ambient conditions, a practical photocatalyst should be active in the visible region ($400 < \lambda < 800$ nm) while also retaining sufficiently positive and negative valence band (VB) and conduction band (CB) edges to carry out redox reactions.[4,21] In the context of aqueous pollutant degradation, the typical purification mechanism involves generating an electron (e^-) hole (h^+) pair to produce reactive oxygen species such as hydroxyl and superoxide radicals from H_2O or O_2, which subsequently go on to attack contaminants until complete mineralization to CO_2 and water (a method classified as an advanced oxidation process (AOP)).[9,22-24] The need to undergo AOPs with

water, preserve a narrow enough band gap to exhibit solar excitation, and remain stable throughout the whole process has made finding an optimal single component photocatalyst problematic.[25] Figure 1.2 displays a series of common metal oxide and sulfide semiconductors, however like TiO_2, all of them have demonstrated difficulties ranging from poor visible light harvesting efficiency (TiO_2, ZrO_2, ZnO), incompatible band edges for AOPs (WO_3, Si, Fe_2O_3), or poor photostability (CdS).[21]

While a 'one size fits all' photocatalyst seems out of reach, there has been extensive interest within the scientific community to find ways to overcome these issues by other means. One such method is through the integration of these materials into alloys or binary/ternary composites, and another is by taking advantage of the surface area and optical properties that can arise when they are organized into certain morphologies. In the case of the former, research has shown that linking semiconductors directly or bridging them together with a mediator can adjust band edges, extend the range of absorbable wavelengths, and facilitate electron transfer, thereby improving electron-hole separation and preventing undesirable recombination.[4,26] In the case of the latter, photonic crystals (PCs) possess both a high surface area and can enhance a materials light absorption ability as a result of the 'slow photon effect' that arises due to Bragg's diffraction.[27,28]

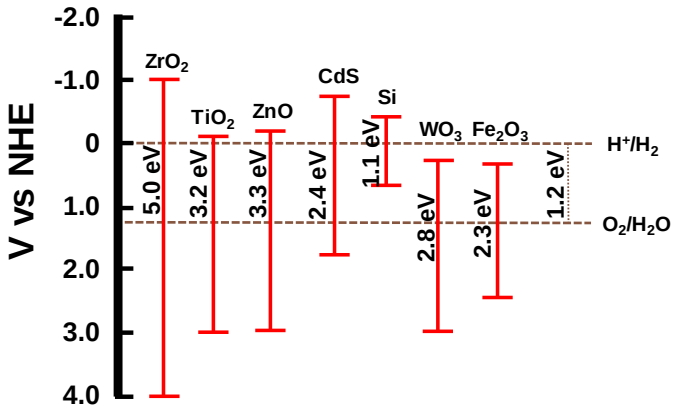

FIGURE 1.2 Relative band edges for various semiconducting materials against a normal hydrogen electrode.[21]

Consequently, the objective of this thesis work is to design visible light sensitive inverse opal (*io*) TiO_2 based binary and ternary systems and investigate their proficiency for the degradation of the azo dye trypan blue (TryB) as an organic pollutant analog in water. The second and third components to be used consist of the narrow band gap semiconductor cadmium sulfide (CdS) and gold nanoparticles (AuNPs) which exhibit localized surface plasmon resonance (LSPR). To simplify extraction, the photocatalysts will be fabricated as thin films on glass slides which can simply be removed from decontaminated water without the need to centrifuge and filter slurries typical of TiO_2 powders. The resulting binary and ternary systems, labeled *io*TiO_2-Au, *io*TiO_2-CdS, and *io*TiO_2-Au-CdS, are expected to possess enhanced photocatalytic activity over unary systems (*io*TiO_2 and CdS) for the reasons mentioned above, and are tested under ultraviolet and visible lighting conditions. This thesis will be structured follows: Chapter 1 will review literature and cover important concepts to heterogeneous catalysis and multiple component photocatalytic systems, Chapter 2 will detail method development for the fabrication of the thin films with final procedures and describe the photocatalytic reaction setup, Chapter 3 will discuss relevant characterization data for the unary, binary, and ternary systems, and Chapter 4 will compare their photocatalytic degradation efficiency against trypan blue under UV and visible light.

1.2 Inverse Opals: Photonic Band Gaps and the Slow Photon Effect

A critical feature that governs efficiency in heterogeneous catalysis is the solid-liquid interface between the catalyst and reacting materials. The interface serves as both the site of reaction and, in the case of photocatalysis, the site for light absorption.[29] Thus,

utilizing small particle sizes or highly porous morphologies is often a straightforward avenue for optimizing photocatalytic efficiency. Inverse opal PCs, which consist of highly ordered close packed arranged voids (Figure 1.3), exhibit high porosity and surface area, as well as another interesting property, referred to as a photonic band gap (PBG). PBGs arise when periodic structures with modulating dielectric constants are arranged on the length scale of visible light and allow PCs to influence light propagation through a material in a manner analogous to how semiconductors regulate current with electronic band gaps.[30,31] The electromagnetic wave equation, like the Schrödinger equation, is an eigenvalue problem with discrete solutions that are all orthogonal.[32] Using the variational method, the lowest energy state for a wave traveling through a periodic lattice must minimize Equation 1:

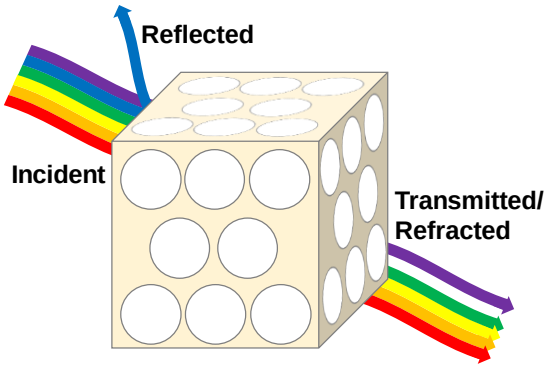

FIGURE 1.3 Illustration of an inverse opal photonic crystal exhibiting light reflection due to a photonic band gap

$$\left(\omega_{n,\vec{k}}\right)^2 \Rightarrow \min_{\vec{E}_{n,\vec{k}}} \frac{\int \left|(\vec{\nabla}+i\vec{k})\times\vec{E}_{n,\vec{k}}\right|^2}{\int \varepsilon \left|\vec{E}_{n,\vec{k}}\right|^2} c^2 \qquad \text{Eq. 1}$$

In brief, this minimum occurs when the dielectric constant (ε) (i.e. the denominator) is high, denoting that the lowest order wave (referred to as the dielectric band) prefers high dielectric regions (Figure 1.4). Since the next order wave must be orthogonal to the first, it is most intense in low dielectric regions and is accordingly referred to as the air band.

These constraints that the waves possess the same periodicity but different average refractive indices (n), imply the waves must have different frequencies (ω). The region

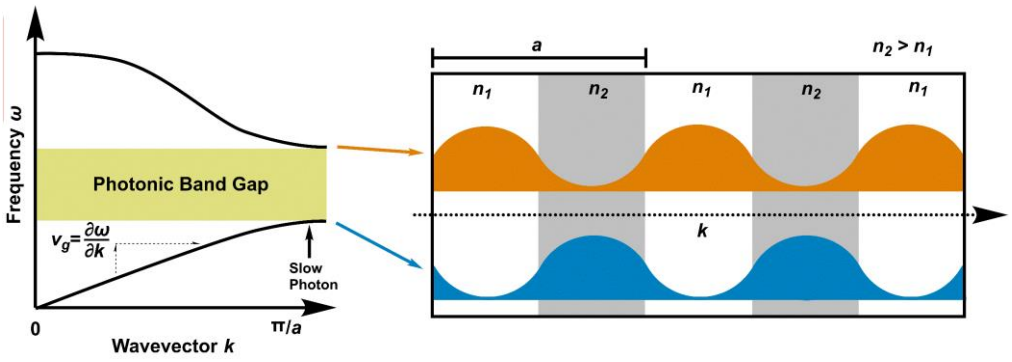

FIGURE 1.4 Origin of the photonic band gap. (Left) Representative band diagram illustrating the gap that arises between frequencies in a photonic crystal. The slope of the line reflects the group velocity (v_g) for the wave, which approaches zero along the edges of the PBG. (Right) One-dimensional wave propagating through a periodic crystal with modulating refractive index *n* along wavevector *k*. The dielectric band (blue) has most of its intensity where *n* is high, the air band (orange) is most intense where *n* is low.

between these frequencies is a range of energies that cannot propagate through the material but are instead reflected away. While reflecting light in and of itself is not useful for photocatalysis, light frequencies along the edges of the PBG experience reduced group velocity (v_g) which has the effect of increasing the path length for light traveling through the material.[31,33] Since the position of the PBG depends on the size of the periodic subunits, the light frequencies that are reflected, and consequently which frequencies are slowed, can be tailored by modifying the size of the voids. Controlled design of the void sizes to utilize the 'slow photon effect' has been shown to be able to enhance the photocatalytic efficiency of materials. Ozin and coworkers evaluated the photocatalytic performance of *io*TiO_2 with different PBG positions for the degradation of methylene blue and found a band gap at 345 nm exhibited an enhancement factor of 1.9 relative to nanocrystalline (*nc*) TiO_2 under 370 nm irradiation normal to the film.[31] Chen et al. prepared inverse opal TiO_2/SnO_2 composite membranes and found the closer the PBG matched titania's electronic band gap the better the photocatalyst performed, with the PBG centered at 370 nm outperforming PBGs at 415 nm, 525 nm, and *nc*TiO_2 for the degradation of rhodamine

B.[34] These PBGs originate from void sizes between 200 – 300 nm. The typical method for fabricating inverse opals is by coating a nanosphere template with a TiO_2 precursor and calcinating to both remove the template and anneal the TiO_2.[35] However, due to the 10% - 25% length contraction the crystal lattice undergoes during the cooling process, polymer templates used typically range between ~220 – 330 nm in size.[36,37] For this project, we will utilize inverse opal structures within that scale.

1.3 Binary Systems: Sensitization with Surface Plasmons and Quantum Dots

Incorporating TiO_2 into binary systems can bring about several advantages. The first is sensitization where a second component, typically an organic chromophore or a noble metal that exhibits localized surface plasmon resonance (LSPR), acts as an 'antenna' for light absorption (Figure 1.5a).[20] In the case of LSPR, when the frequency of light incident to a noble metal nanoparticle matches the frequency of its surface electron oscillations, the light is absorbed, and excitation occurs. Gold and silver nanoparticles

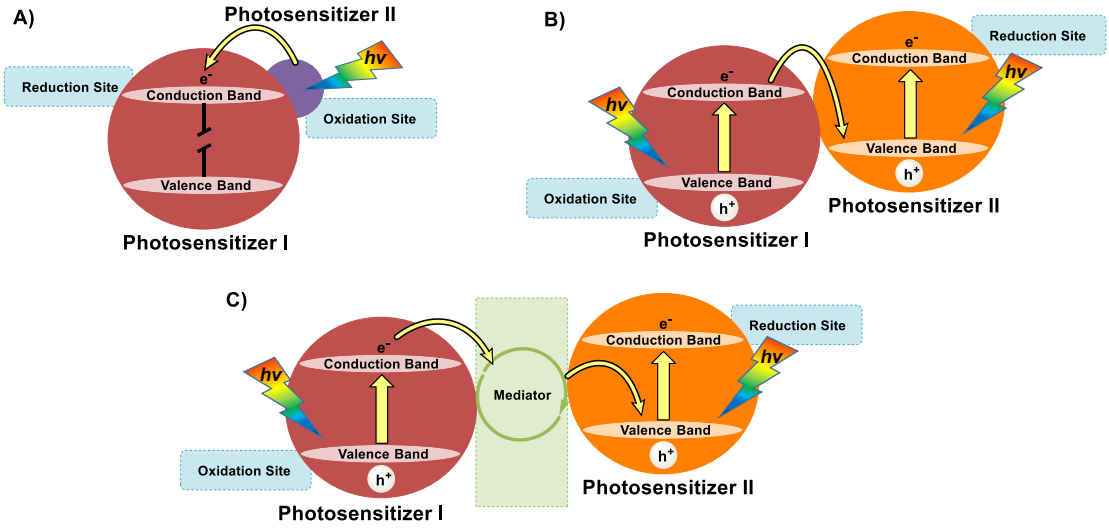

FIGURE 1.5 Generalized photocatalytic reaction mechanisms for A) binary sensitization, B) binary Z-scheme, and C) ternary Z-scheme.

exhibit surface electron resonance at frequencies within the visible spectrum, and thus absorb in the visible region, with the exact frequency of absorption depending on the nanoparticle's size and shape.[38] These excited, 'hot' electrons readily transfer into the CB of TiO_2 where they can subsequently be used for redox.[39]

Sensitization effectively broadens the range of wavelengths that a photocatalyst can utilize, and has been shown to improve the photocatalytic activity of TiO_2 under visible light, especially in cases where titania's PBG aligned with the nanoparticle's λ_{LSPR}. Wang et al. demonstrated enhanced visible light performance for TiO_2-Au biomorphic photonic crystals (BMPCs) over P25 titania.[20] The BMPCs were made using butterfly wings as a template and possessed a PBG that synergized with the LSPR of the embedded gold nanoparticles, resulting in improved degradation efficiency of methyl orange. Lu et al. infiltrated 240 nm *io*TiO_2 PCs with 15 nm AuNPs and found the enhanced visible light absorption gave the binary system a 2.3-fold larger kinetic constant over *nc*TiO_2 for the degradation of 2,4-dichlorophenol.[40] Similarly, Zhao et al. synthesized AgNPs *in situ* on *io*TiO_2 thin films and found the apparent rate constant for the degradation of methylene blue was 4.2 times higher than a conventional *nc*TiO_2-Ag film and 36 times higher than *nc*TiO_2 by itself under visible light.[41]

In addition to sensitization, coupling TiO_2 with narrow band gap semiconductors has been another much-investigated avenue for improving titania's photocatalytic efficiency. Semiconductors with electronic band gaps between 1.5 – 3.0 eV can absorb in the visible spectrum, and depending on relative band edge positions, can exchange excited electrons with TiO_2 in a similar manner to noble metal nanoparticles.[42-44] However, more interestingly, coupling semiconductors allows the tasks of reducing and oxidizing water to

be split between the two photosensitizers in a process called Z-scheme photocatalysis (Figure 1.5B).[45] This is advantageous because it circumvents the requirement of needing a single material capable of both halves of water redox and the charge transfer between semiconductors increase electron-hole separation which inhibits recombination.[26] Taken in conjunction these factors widen the scope of viable sensitizers to include those that individually have difficulties performing photocatalysis either due to poor band gap alignment or high rates of recombination.

Examples of narrow band gap semiconductors that have been utilized include $CuInS_2$ (1.5eV),[46] Cu_2O (2.0 eV),[47] $ZnFe_2O_4$ (1.86 eV),[48] and CdS (2.4 eV).[49] CdS in particular has seen extensive use due to its ideal electronic band width and positioning. Pant et al. embedded TiO_2-CdS nanoparticles onto carbon nanofibers and tested for the degradation of 10 ppm solutions of methylene blue, reactive black 5 and reactive orange 16 under sunlight. In addition to the absorption caused by the carbon content of the fibers, the photocatalytic activity of the TiO_2-CdS binary system improved the rate of dye degradation.[49] Xia et al. modified CuO inverse opals with CdS to make a glucose biosensor and found that addition of QDs improved the electrode's sensitivity to glucose addition over plain *io*CuO and CuO thin films.[27] Fujishima et al. sensitized mesoporous *nc*TiO_2 films with CdS using a photocatalytic growth of preformed seeds (PCGS) technique and tested the systems proficiency at photocatalytic hydrogen generation.[44] The electrochemical cell exhibited an increase in H_2 generation under simulated sunlight as TiO_2 surface coverage increased. For this project, we utilize AuNPs or CdS QDs as photosensitizer II (PSII) coupled to *io*TiO_2 photosensitizer I (PSI). For the reasons given

above, the addition of the second photosensitizer is expected to enhance the photocatalytic performance of TiO_2 under ambient conditions.

1.4 Ternary Systems: Electron Mediators in Z-Scheme Photocatalysis

Expanding on the same concepts as binary systems, ternary Z-scheme systems use two photosensitizers bridged together with an electron mediator (Figure 1.5C).[4,26] Like the binary systems, addition of a narrow band gap semiconductor for PSII increases the range of usable wavelengths for photocatalysis and allows the tasks of reduction and oxidation to be split between the two components.[45] The key difference in ternary systems however is the presence of an electron mediator which facilitates electron transport between the two photosensitizers. The mediator, which can be an electrolytic solution in aqueous phase or a conductive material in solid state, further improves electron-hole separation by offering a low resistance pathways from CB_{PSI} to VB_{PSII} or CB_{PSII} to CB_{PSI}.[26] Additionally, the mediator can act as a third point of electron excitation if it exhibits visible light absorption in and of itself, such as in the case of plasmonic nanoparticles, where AuNPs have been shown to be capable of both shuttling between and injecting photoexcited 'hot' electrons to coupled photosensitizers.[39]

Typical examples of mediators used in ternary Z-schemes include reduced graphene oxide,[45] AuNPs,[39,50] AgNPs,[51] and tungsten.[52] Iwase et al. demonstrated the ability of reduced graphene oxide sheets to act as an electron shuttle between $BiVO_4$ and $Ru/SrTiO_3$:Rh photocatalysts for enhanced water splitting.[45] The mediator tripled the amount of generated H_2 compared to the two photocatalysts coupled without it (3.7 µmol to 11 µmol). Lin et al. composed an all silver Z-scheme system, which was comprised of AgBr and AgI as PSI and PSII respectively with AgNPs acting as the mediator.[51] In

photocatalytic experiments for methyl orange degradation in visible light, the ternary system outperformed Ag-AgI and Ag-AgBr binary systems.[51] For our ternary system, we incorporate all three of our binary photosensitizers, TiO_2, AuNPs, and CdS QDs, into an *io*TiO_2-Au-CdS composite system with TiO_2 and CdS acting as PSI and PSII respectively, and AuNPs acting as the electron mediator.

CHAPTER 2. MATERIALS AND METHODS

2.1 Materials

Cadmium acetate dihydrate (98%) was purchased from Arcos Organics. Crystalline L-ascorbic acid (99.6%), hydroquinone, and Sodium citrate dihydrate were purchased from Fischer Scientific. Polyvinylpyrrolidone (average MW 40000) (PVP), sodium sulfide nonahydrate (98.0%), sodium tetrachloroaurate (III) dehydrate (99%), titanium(IV) bis(ammonium lactate) dihydroxide (50% wt. % in H_2O) (TiBALDH), styrene monomer, stabilized (99%), methyl methacrylate monomer, stabilized (99%), 2,2'-Azobis(2-methylpropionamidine) dihydrochloride (97%) (AIBA) and trypan blue (TryB) were purchased from Sigma-Aldrich. Sodium borohydride (≥99%) was purchased from Fluka Analytical. All chemicals and solvents were used as received.

Our generalized approach, illustrated in Figure 2.1, was to fabricate the *io*TiO_2-Au-CdS complex bottom up by the coassembly of a polystyrene (PS) or poly(methyl methacrylate) (PMMA) nanosphere sacrificial template with a water soluble titania

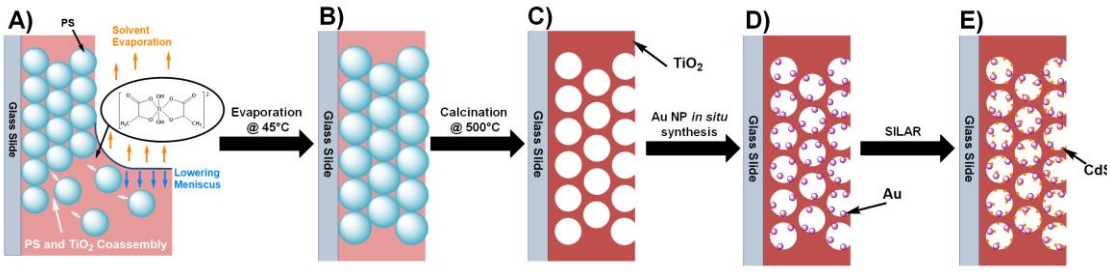

FIGURE 2.1 *io*TiO_2-Au-CdS fabrication outline illustrating (A-B) coassembly of polymer nanospheres and TiBALDH, (C) removal of polymer, (D) in situ synthesis of AuNPs, and (E) SILAR deposition of CdS QDs

precursor (titanium(IV)- bis(ammonium lactate) dihydroxide or TiBALDH) (Figure 2.1A-B) followed by calcination of the polymer scaffolding (Figure 2.1C), *in situ* synthesis of the gold nanoparticles (Figure 2.1D), and deposition of CdS quantum dots by successive ionic layer absorption and reaction (SILAR) method (Figure 2.1E). The justification for the methods used and detailed procedures are specified below.

2.2 Synthesis of Polystyrene and Poly(methyl methacrylate) Nanospheres

PS nanospheres approximately 250 nm in size were synthesized by surfactant free emulsion polymerization following literature procedure.[53] The size of the nanoparticles can be regulated by controlling the concentrations of the initiator, stabilizer, and monomer. A 100 mL two-necked round bottom flask was placed in a sand bath and fastened with a reflux condenser and a thermometer. The joints were wrapped in Teflon tape to prevent PS from fusing the condenser and the round bottom together during the reaction. A rubber septum was placed onto the reflux condenser and nitrogen was pumped to a gas bubbler to make the atmosphere inert. Polymerization was carried out by first dissolving 0.0651 g AIBA initiator, 0.6 g PVP stabilizer, and 5.518 mL styrene monomer in DI water and diluting to 50 mL. The reaction chamber was sealed under nitrogen and slowly heated to 70-80˚C where it was held for 6 hours with stirring. After polymerization, the latex beads were washed by centrifuging at 13000 rpm for 20 minutes 3-4 times, dispersed in 40 mL DI water, and sonicated for 30 minutes to break up agglomerates.

~200 nm PMMA nanospheres were synthesized and treated in a similar manner,[53] using 0.015 g AIBA, 3.0 mL methyl methacrylate monomer, 16 mL DI water and no stabilizer. In addition, 600 nm 10% PS beads were purchased from Sigma-Aldrich and

diluted in DI water as necessary. Nanospheres were imaged by scanning electron microscopy and average particle diameter was measured using imageJ software.[54,55]

2.3 Fabrication of Inverse Opal TiO_2 by Coassembly

Initial efforts to fabricate inverse opals were done using typical 2-step fabrication techniques from literature.[56,57] In these, the polymer nanosphere template was first deposited onto the slides by flow controlled vertical deposition with a peristaltic pump or by evaporation at 45°C. The gradually lowering meniscus caused the nanospheres to adhere to the surface of the glass slide in a arrangement, after which the nanosphere template was infiltrated with a TiO_2 sol-gel by dip coating or drop casting. The slides were then calcinated at 500°C to remove the template and anneal the titania yielding inverse opals. Unfortunately, many of these 2-step procedures suffered from complications such as polymer template damage during infiltration, large over-layers of TiO_2 on top of the inverse opals, or films that would flake off the slide easily, resulting in poor surface coverage (Figure 2.2). Additionally, the polymer deposition process needed to be slower than the available peristaltic pump allowed to ensure proper self-assembly, thus all succeeding PC templating processes were done via evaporation over the course of 1 – 2 days.

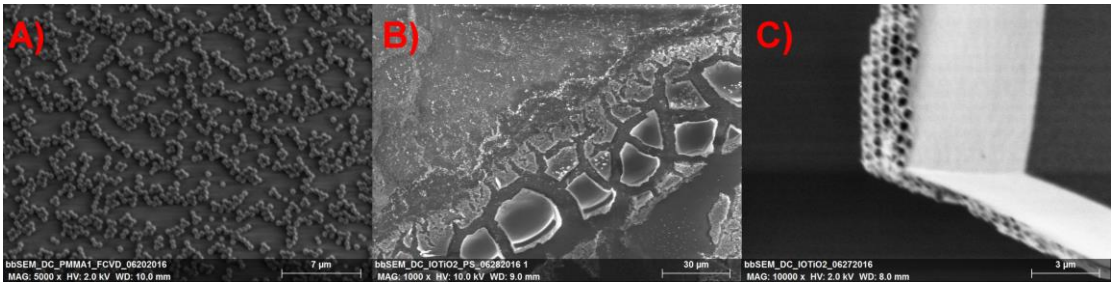

FIGURE 2.2 Examples of typical defects during inverse opal fabrication. A) Disordered PMMA nanospheres due to fast vertical deposition process not permitting self-assembly. B) "Shoreline" pattern where PS template was washed away during infiltration with titania precursor. C) Solid TiO_2 over-layer when excess sol gel was deposited onto template.

We eventually transitioned from 2-step methods to a simplified coassembly method taken from literature which involved simultaneously depositing the polymer template with a water soluble titania precursor.[37,58-60] This both saved time due to no longer requiring a separate infiltration step, and yielded good surface coverage without flaking or over-layers. The finalized procedure went as follows, glass microscope slides (0.83x1.88 cm) were cut, rinsed with isopropanol, and soaked in piranha solution for 30 - 60 minutes to clean and make them hydrophilic. The clean slides were stored in DI water until ready to use. The coassembly mixture consisted of 1 mL 2.5% wt PS, 160 µL 50% TiBALDH, and 2.840 mL DI water. One slide was placed in a vial (ID ~2 cm) and was submerged in the coassembly mixture. The vials were left in a 45˚C incubator for 1-2 days to evaporate, then were subsequently calcined at 500˚C for 3 hours using a temperature ramp rate of 2˚C/min in a muffle furnace. After heating, the slides were cooled naturally to room temperature. Films were characterized with SEM, EDX, solid state UV-visible, and Raman spectroscopies. Pore sizes were measured with imageJ. [54,55]

2.4 In situ Synthesis of AuNPs using Different Reducing Agents

First attempts to incorporate gold nanoparticles into the inverse opal structures involved drop casting a known volume and concentration of AuNPs onto the surface of the slides, however this technique resulted in the gold nanoparticles coalescing along the edges of the drop due to the "coffee ring effect" (Figure 2.3).[61,62] To ensure uniform distribution of nanoparticles we developed an *in situ* synthesis method involving the reduction of gold chloride with various reducing agents

FIGURE 2.3 The "coffee ring effect" during AuNP drop casting

in the presence of the thin film, with and without citrate acting as a capping agent (Figure 2.4). The reducing agents used were 100 mM ascorbic acid, 100 mM $NaBH_4$, and 30 mM hydroquinone. The *io*TiO_2 slides were taped to the wall of a vial with Kapton tape and immersed in a mixture of 5.940 mL DI water and 60 µL 25 mM $AuCl_4^-$ with stirring. Solutions with citrate used 4.913 mL DI water with 37 µL 34 mM citrate and the same amount of $AuCl_4^-$. After soaking for 30 minutes, 180 µL L-ascorbic acid, 180 µL $NaBH_4$, or 60 µL hydroquinone was quickly injected while stirring was sustained for another 15 minutes, after which the nanoparticle solution was covered and allowed to age overnight. The slides were removed from the gold solutions the next day, briefly rinsed with DI water, and dried in an 80°C oven. AuNPs containing slides were characterized with SEM, EDX, and solid state UV-vis. Particle sizes were measured with imageJ. To demonstrate repeatability, residual AuNPs solutions were characterized by UV-visible spectroscopy.

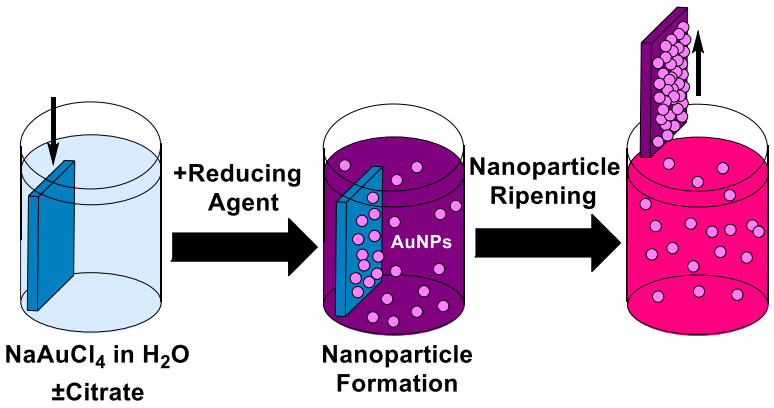

FIGURE 2.4 in situ AuNP synthesis outline

2.5 CdS Deposition by SILAR Method

CdS layers were applied by following a modified SILAR method from the literature per Figure 2.5.[17,27,63,64] 50 mM solutions of $Cd(Ac)_2 \cdot 2H_2O$, and $Na_2S \cdot 9H_2O$ were prepared in ethanol and 25%:75% water-to-methanol respectively. First, a slide was soaked in the Cd^{2+} solution for 30 seconds to absorb cadmium ions before being moved to a beaker containing pure methanol for 30 seconds to rinse off excess cadmium and acetate ions. The slide was dried under an N_2 stream and then soaked in the S^{2-} solution for 30 seconds to allow sulfide to react with the absorbed cadmium ions and form CdS. The slide was rinsed again in another beaker of clean methanol then dried under N_2, thereby completing one cycle. SILAR cycles were performed 10 times on clean slides for unary CdS thin films and on slides containing *io*TiO_2 and *io*TiO_2-Au to produce the binary and ternary systems. CdS containing slides were characterized with SEM, EDX, solid state UV-visible, and Raman spectroscopy. Particle sizes were measured with imageJ.

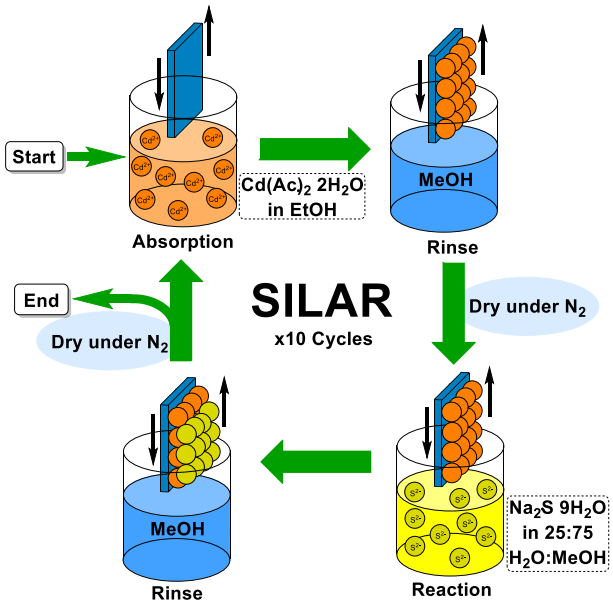

FIGURE 2.5 Modified SILAR procedure illustration for deposition of CdS QDs. 10 cycles were performed on each CdS containing slide.

2.6 Photocatalytic Tests

Trypan blue was selected as our pollutant analog on the basis that azo dyes make up an estimated 50% - 70% of global dye production and are classified under Group 2B as possible carcinogens by the International Agency for Research on Cancer.[65-67] Preliminary reactions (Figure 2.6) were performed by placing slides in a beaker with 25 mL 20 µM

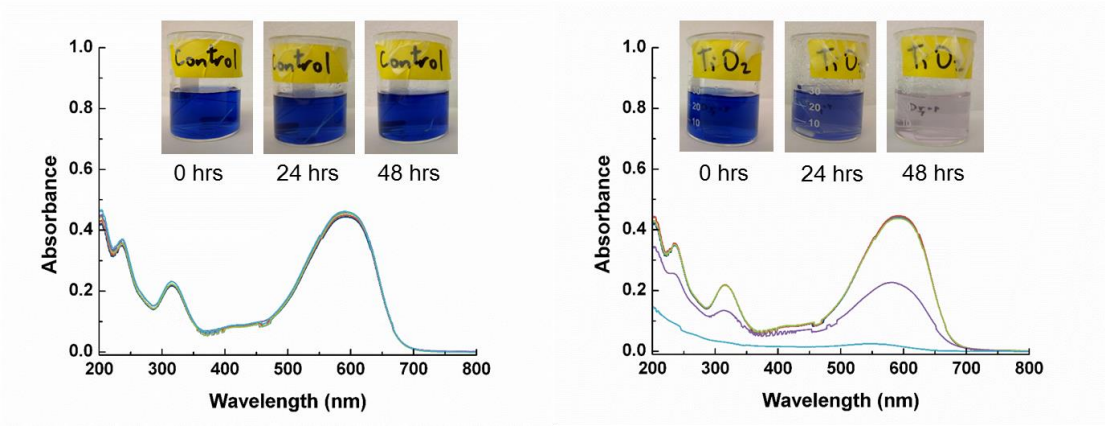

FIGURE 2.6 Preliminary photocatalytic degradation of 20 µM trypan blue under UV light using a clean slide control (left) and nanocrystalline TiO_2 (right). Reactions performed with ~0.2 mg catalyst in 25 mL dye solution.

TryB under ultraviolet light, however, the amount of catalytic material per slide was found to be approximately 0.2 mg, yielding a final concentration of 8 µg/mL. In these conditions, the low catalyst loading and long passive diffusion distance due to lack of solution agitation severely limited the rate of reaction to an excess of 48 hours and made a direct comparison of photocatalytic performance impractical. The rigid structure of the slides further complicated choice of reactor setup since the reactor needed to balance using small volumes to maintain reasonable catalyst loading while having sufficient volume to ensure the slide remained submerged at all times. Moreover, the reactor needed to allow for solution agitation to prevent passive diffusion from becoming rate limiting, and be

transparent to our light source. Thus, a major facet of this project was designing an adequate reactor for running thin film experiments.

Some of the attempted reactor designs to solve these problems include a small scale 'shallow pond' reactor (not pictured) where the slide was placed in a vial and air was bubbled in via a peristaltic pump, and a microfluidic inspired 'macrofluidic' device for flowing small (1 - 2 mL) volumes over thin films (Figure 2.7A).[68,69] Nevertheless, there remained difficulties getting the reactors to operate satisfactorily. The former suffered from evaporation becoming a significant variable due to the small volumes used and the fact that the reactor needed to be open to the air for several hours, and the latter from a complicated assembly process and frequent leaks. The reactor that was ultimately used for photocatalytic reactions was a simple acrylic cuvette used for UV-visible spectroscopy measurements (Figure 2.7C-D). The cuvette's dimensions keep slides submerged in 3 mL of dye solution, they are transparent down to 300 nm, allowing them to act as an artificial 'atmosphere' to filter out any trace UVB and UVC rays that may be emitted by the light

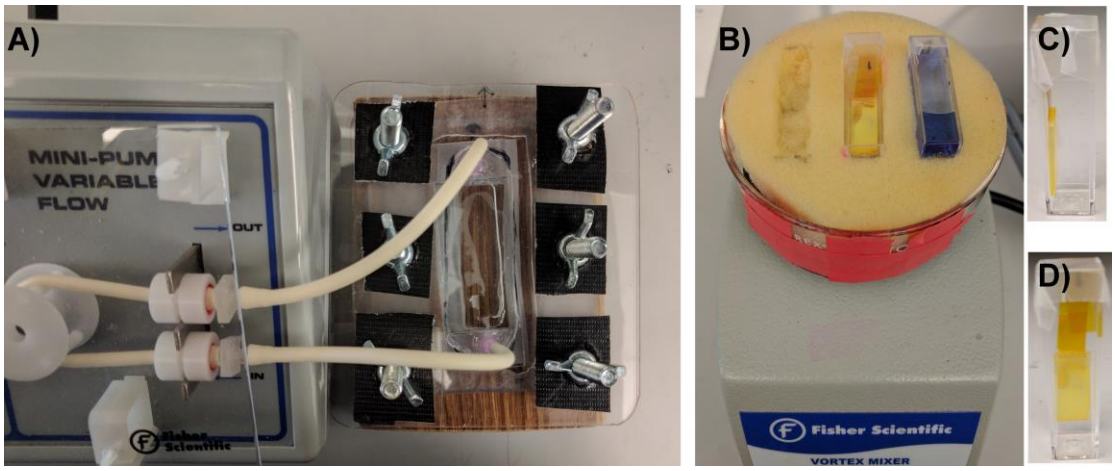

FIGURE 2.7 Reactor development. (A) Custom made macrofluidic device. Slides would be placed in the hollow central cell and solution would be circulated over the films via the peristaltic pump through syringes. (B) Vortex mixing reaction apparatus with cuvettes laying in the foam cushion. (C) Front view of an acrylic cuvette with example *io*TiO_2-CdS slide taped inside. The glass slides are thin enough that they do not block the beam path during UV-vis measurements. (D) Side view of same cuvette.

source, and in being designed for UV-visible measurements the cuvettes could easily be sealed with parafilm and placed directly into the spectrophotometer without the need to extract or transfer liquids, thus reducing labor and negating the chance for spills. Reactions were thus performed by inserting the cuvettes in a foam cushion with holes cut out such that the cuvettes could lay flat with the films facing up. The cushion was then placed in a Pyrex petri dish, taped to a vortex mixer for agitation, and exposed to irradiation (Figure 2.7B).

For irradiation, two light sources were selected: a UV source to observe maximum photocatalytic performance when all three components in the ternary system are expected to be active, and a visible light source to simulate performance under sunlight. The UV source was a low-pressure mercury UV bench lamp (15 watts, peak wavelength 365 nm) with a 400 nm cutoff filter, while the visible source required more careful selection. Typically, expensive xenon arc lamps are used for simulating sunlight due to their comparable spectral power distribution (SPD) profiles. However, we were interested in observing the catalyst's performance under a cheaper alternative. Figure 2.8 displays normalized SPD profiles taken from The National Gallery, London for three representative light bulbs and UV-filtered sunlight.[70] As can be seen, sunlight (orange) possesses uniform and continuous power output across all visible wavelengths. By contrast incandescent bulbs (red) emit

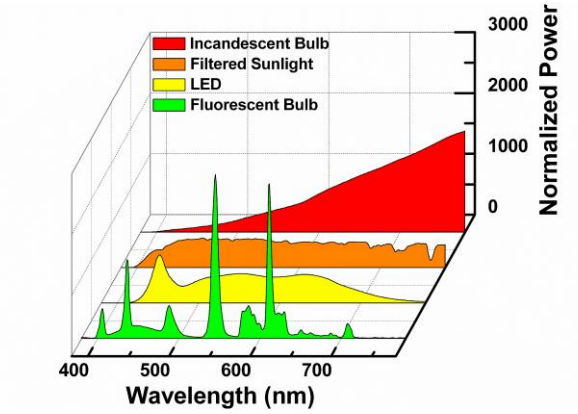

FIGURE 2.8 Normalized spectral power distribution diagram for various light sources, xenon arc lamp profile not included.[70]

primarily from the red to the infrared region while fluorescent bulbs (green) exhibit heavy quantization due to their means of generating light (fluorescence). Recently, there has been growing interest in utilizing light emitting diodes (LEDs) for UV/visible light applications and water treatment due to their low energy cost, long lifespan, and absence of toxic mercury present in traditional UV lamps.[71] Repo et al. successfully used near UV and blue LEDs as light sources for the photocatalytic degradation of methylene blue, phenol red, and methyl red dyes with CdS microspheres.[71] Wang et al. fabricated heterostructured Ag-AgBr/TiO_2 composites and demonstrated their ability to photocatalytically degrade ibuprofen and bacteria under white light LED irradiation.[72] Like sunlight, white light LEDs (yellow) possess continuous SPD profiles that encompass the full visible spectrum and allow them to potentially act as cheap alternatives to customary solar simulators. Hence, for our visible reactions, we make use of a 17-watt white light LED bulb (1600 lumens, color temperature 5000 K)

To summarize, our final procedure for the photocatalytic reactions went as follows: photocatalyst slides were taped to the opaque side of an acrylic cuvette with Kapton tape. 3 mL of 20 μM trypan blue was transferred to the cuvette which was then sealed with parafilm. Slides were left in the dark for 30 minutes to reach adsorption/desorption equilibrium before being placed 5 cm away from the selected light source with solution agitation generated by a vortex mixer. Photocatalytic activity was evaluated by monitoring TryB decolorization with a UV-visible spectrophotometer every 10 minutes for at least 1.5 hours before terminating the reaction.

2.7 Characterization Techniques: Theory and Instrumentation

2.7.1 Principles of UV-Visible Spectroscopy

UV-visible spectroscopy operates by separating a beam of white light into its components via a prism or diffraction grating. The monochromatic beam is then split into two beams of equal intensity that pass through a sample and reference. If the sample absorbs then the intensity of light picked up by the sample detector (I_0) will be less than the intensity of light picked up by the reference detector (I) at that wavelength.[73] Absorbance (A) is defined as the logarithm of the ratio of these two values ($A = Log I_0/I$), thus absorption caused by the sample appears as a peak in the spectrum. The cause of UV-visible absorption in organic molecules typically involves nonbonding to π antibonding ($n \rightarrow \pi^*$) or π bonding to π antibonding ($\pi \rightarrow \pi^*$) electronic transitions present in heavily conjugated molecules (such as trypan blue),[74] however, semiconductors with electronic band gaps between 1.5 – 3.0 eV also exhibit electronic excitation in this range and thus have visible coloration. Because of this a photocatalyst's band gap, and consequently its range of active wavelengths, can be estimated with solid state UV-visible spectroscopy.[75] In addition, nanoparticles with LSPR demonstrate strong absorbance in the visible region which appears as a peak whose λ_{max} and width correlate to average particle size and distribution respectively.[76] For this project, UV-visible spectroscopy was used for characterization and to monitor dye discoloration due to photocatalysis. All UV-vis absorption spectra were recorded using a Cary 4000 UV-visible spectrophotometer.

2.7.2 Principles of Raman Spectroscopy

Raman spectroscopy detects changes in a molecule's vibrational state caused by the inelastic backscattering of monochromatic infrared light.[77] Interactions that result in

reflected light losing energy (and consequently the target molecule gaining energy) are referred to as Stokes shifts while the opposite are referred to as Anti-Stokes shifts (Figure 2.9). Due to the weak intensity of Raman scattering relative to elastic Rayleigh scattering, Raman spectroscopy has low sensitivity, however since Raman scattering depends heavily on a molecule's bonds and symmetry, a Raman spectra can act as a 'fingerprint' unique to a given molecule. Raman spectra were taken with a portable BWS415-785S *i*-Raman from BWTEK using a diode laser with a 785 nm excitation wavelength. The instrument was connected to a BAC-151B video microscope for visualization with a 20x objective lens set at an 8.8 mm working distance. Raman shift resolution was < 4.5 cm^{-1}. Measurements were taken using laser power ranging from 20% - 60% (max 320 mW), integration times from 150 – 5000 ms, and a time average of at least 20 spectra.

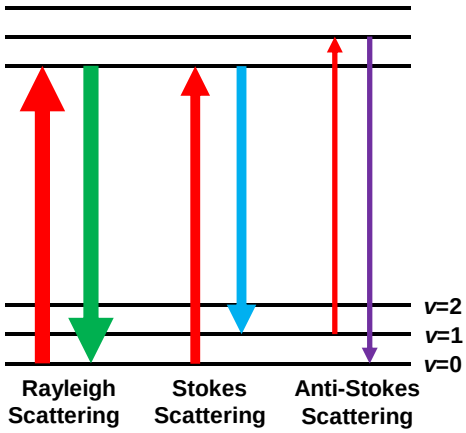

FIGURE 2.9 Rayleigh and Raman scattering. Line width correlates to intensity

2.7.3 Principles of Scanning Electron Microscopy and Energy Dispersive X-ray Analysis

Scanning electron microscopy (SEM) operates by heating a tungsten filament (the electron gun) to overcome the metal's work function and induce electron flow.[78] This beam of primary electrons travels through a series of lenses which focus the beam until contact with the sample, after which several types of interactions can occur. Secondary electron imaging mode uses electrons that are inelastically scattered by primary electrons (i.e. secondary electrons) in a raster scan pattern to form a digital image of the sample. The

instrument correlates the brightness of a single pixel in the image to the number of secondary electrons detected at that spot in the sample. The number of secondary electrons emitted by the sample depends on its geometry, with edges, curves, and slopes emitting more electrons than flat surfaces normal to the primary beam, and thus appearing brighter. After taking a scan of a single spot on the sample, the beam moves over slightly and takes another, thereby filling in the next pixel in the image. This process can be repeated over the course of a set area to yield a two-dimensional projection of the samples three-dimensional surface. While most scattering involves primary electrons colliding with valence electrons, occasionally a primary electron will knock an inner electron out of place.[78] To fill the hole an electron at a higher energy level relaxes, thereby emitting an X-ray. X-rays emitted from n=2→1 transitions (L shell to K shell) are Kα X-rays, n=3→1 (M→K) are Kβ, n=3→2 (M→L) are Lα, n=4→2 (N→L) are Lβ, and so on (Figure 2.10).[78] The exact energy of an X-ray emission depends on the difference between the two energy levels and the element's atomic number, and as such it is characteristic of a given element. Detection with an energy dispersive X-ray spectrophotometer (EDX) can identify elemental components in a sample and determine relative weight and atom percent compositions.

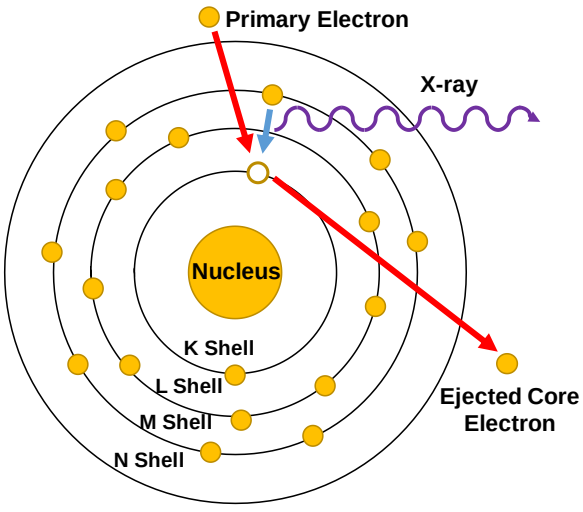

FIGURE 2.10 Principles of EDX. Characteristic X-ray emission after ejection of a core electron

In-house SEM images and EDX spectra were collected from a JEOL JSM5800LV SEM EDX at an accelerating voltage of 3 - 10 keV. Samples were mounted onto an

aluminum stub with copper tape and placed into the instrument in secondary electron imaging mode (SEI) for imaging or back-scattered electron mode (BSE) for elemental analysis. Out of house images were taken by Emory University's Robert P. Apkarian Integrated Electron Microscopy Core for TEM and FE-SEM analysis with a Topcon DS150 Field Emission Scanning Electron Microscope (FE-SEM) at 10 kV in secondary electron mode. Samples were cut into small 5 mm x 5 mm squares, sputter coated with 15 mm chromium using a Denton DV602 magnetron sputter coater, and fixed onto an aluminum labeled upper stage for imaging.

CHAPTER 3. FABRICATION AND CHARACTERIZATION

3.1 Inverse Opal TiO_2 Thin Film Construction

SEM imaging shows polymer templating by evaporation was successful at yielding close packed ordered nanospheres (Figure 3.1). The polymer films exhibit strong iridescence attributed to the PCs' structural coloration.[79] The specific color of the film corresponds to the size of the nanospheres and can be seen in the insets of Figure 3.1. ~200 nm PMMA is blue, ~250 nm PS is green, and 600 nm PS is red.

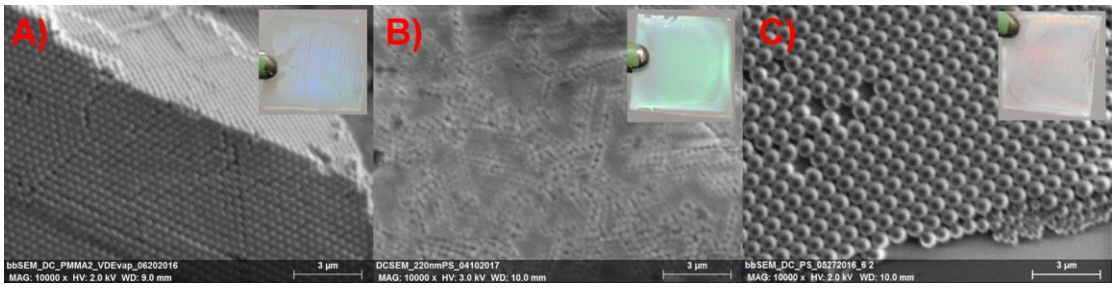

FIGURE 3.1 SEM images for polymer nanosphere templates by evaporation at x10k magnification. (A) ~200 nm PMMA, (B) ~250 nm PS, (C) 600 nm PS.

Utilizing the polymer suspensions for coassembly resulted in good inverse opals without over-layers as can be seen in Figure 3.2. In addition to these areas however, there are also extensive regions on the slide with cracking which is likely attributed to different rates of expansion and contraction between the substrate and thin film during the heating and cooling process(Figure 3.2E and D).[37,58,60] Overall, the films adhere strongly onto the glass substrate with no flaking and still exhibit structural coloration, albeit with reduced intensity due to crystal defects. PMMA-*io*TiO_2 is white, 250 nm PS-*io*TiO_2 is a faint blue, and 600 nm PS-*io*TiO_2 is faint green.

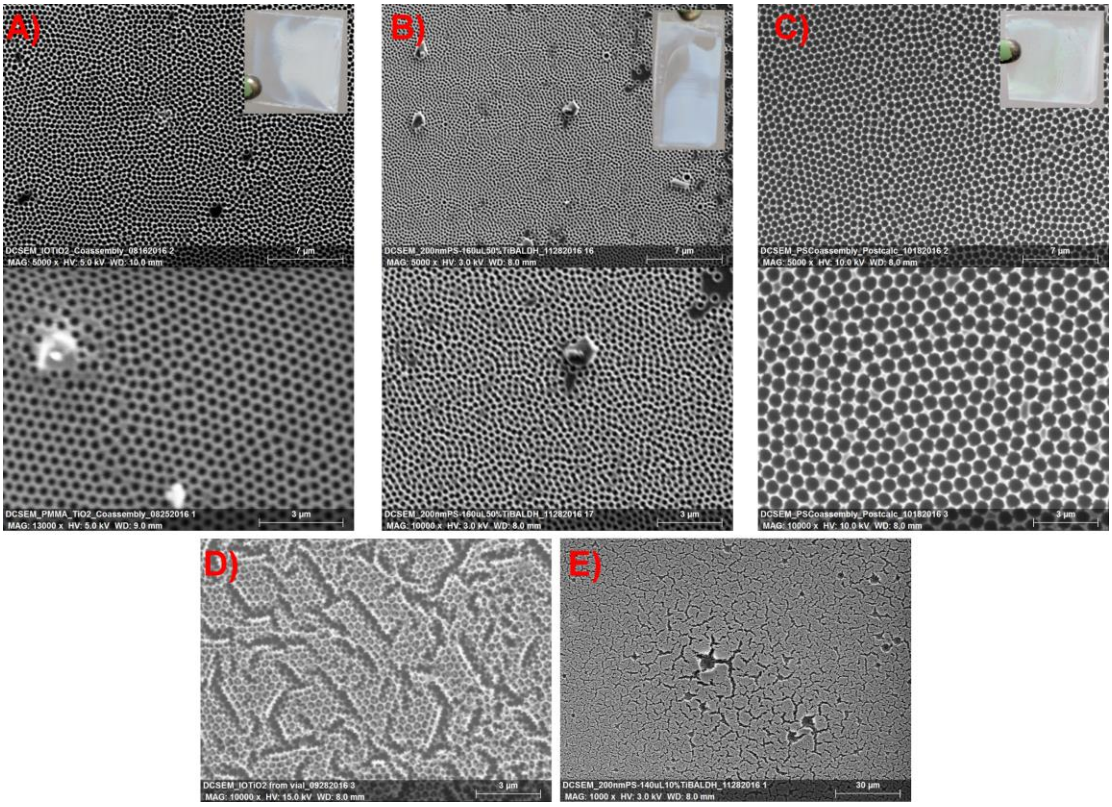

FIGURE 3.2 *io*TiO_2 from different polymer templates at two magnifications. (A) ~200 nm PMMA at x5k (top) and x13k (bottom), (B) ~250 nm PS at x5k (top) and x10k (bottom), and (C) 600 nm PS at x5k (top) and x10k (bottom). (D and E) Examples of cracking seen commonly in inverse opal films and x10k and x1k magnification. Note, the inverse opals are too small to see in E.

While all polymer templates yielded inverse opals, due to better availability the ensuing experiments make use of the ~250 nm PS template exclusively for PC fabrication.

3.2 In situ Synthesis of AuNPs

To ensure thorough coverage of the inverse opals, AuNPs were synthesized *in situ* using different reducing agents, with or without citrate. The resulting solutions and *io*TiO_2-Au slides are depicted in Figure 3.3. The only conditions that yielded substantial AuNPs growth were in presence of ascorbic acid without citrate as evidenced by the film's change

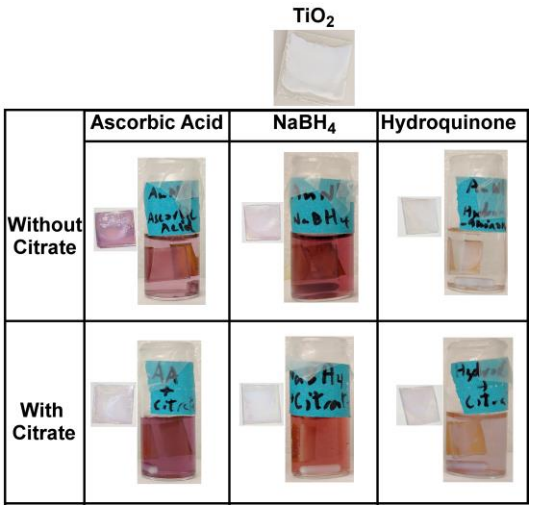

FIGURE 3.3 In situ AuNP synthesis with various reducing agents compared to *io*TiO_2.

in color to purple. By contrast, the film in presence of sodium borohydride only exhibited a slight change in coloration while hydroquinone failed to produce AuNPs on *io*TiO_2. The addition of citrate appeared to interfere with nanoparticle growth on the *io*TiO_2 lattice as can be most evidently seen in the case of ascorbic acid + citrate, where there is very little color change from that of TiO_2.

Due to the small size of the nanoparticles, the in-house SEM is not capable of determining size distribution. However, as a way of indirectly ensuring reproducibility for the *in situ* synthesis, UV-visible spectra were taken of the residual nanoparticle solutions

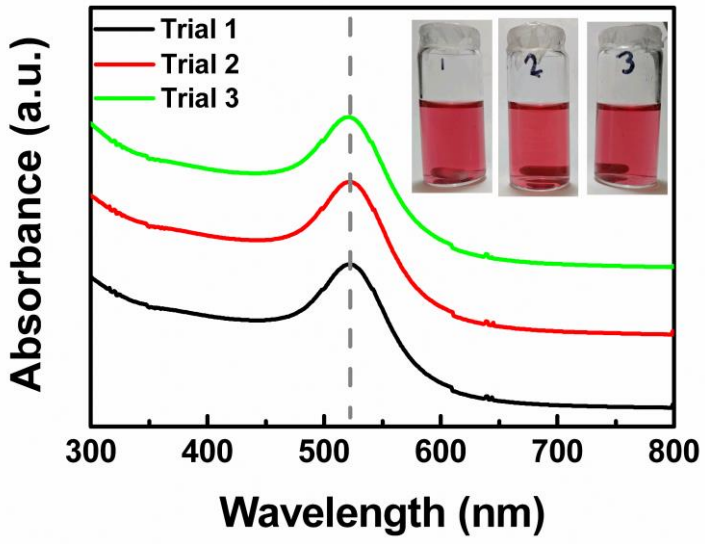

FIGURE 3.4 Residual in situ AuNP solution UV-visible spectra for three separate trials. (inset) digital images of the solutions after removing the glass substrate. λ_{LSPR} was 522 (±1) nm for the three trials.

from three separate trials using ascorbic acid as the reducing agent (Figure 3.4). The average λ_{LSPR} was 522 ±1 nm between the three trials suggesting good reproducibility.

3.3 SEM/EDX Analysis and Size Distributions

After growth of the AuNPs, CdS QDs were deposited onto non-functionalized glass, *io*TiO_2, and *io*TiO_2-Au yielding the remaining unary, binary, and ternary systems. High resolution FE-SEM images of each of the thin films were collected at Emory University's electron microscopy facility and are displayed in Figure 3.5 along with digital image insets. The unary CdS thin film was transparent yellow in color, while the *io*TiO_2-CdS binary system was orange-yellow and opaque due to titania's presence. Addition of the CdS QDs to the *io*TiO_2-Au binary system turned the film a dark green/black color.

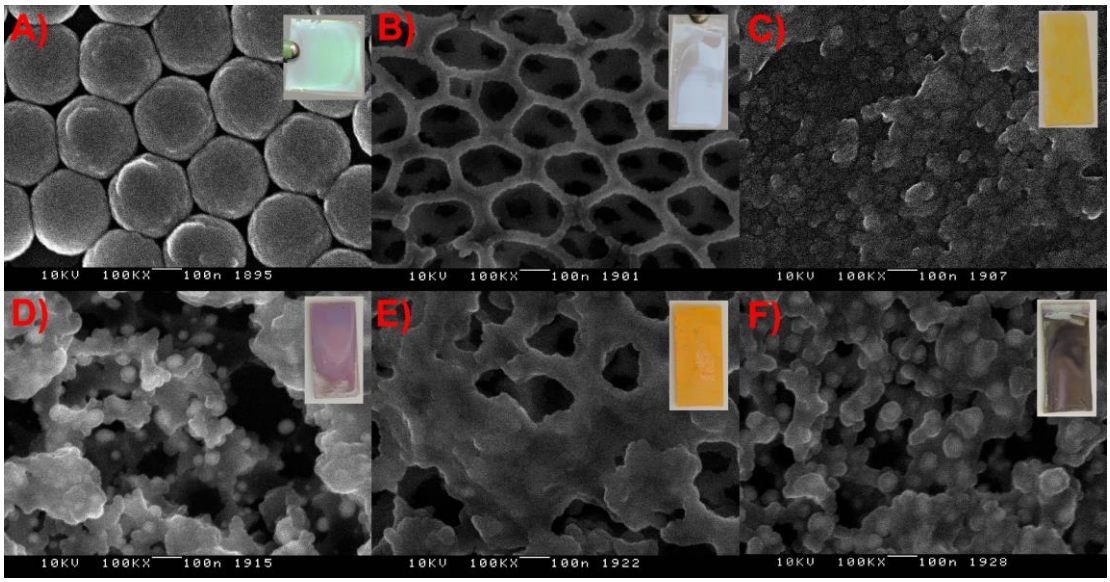

FIGURE 3.5 FE-SEM and accompanying digital images of composite materials, taken at x100k magnification. (A) Polystyrene, (B) *io*TiO_2, (C) CdS thin film, (D) *io*TiO_2-Au, (E) *io*TiO_2-CdS, and (F) *io*TiO_2-Au-CdS.

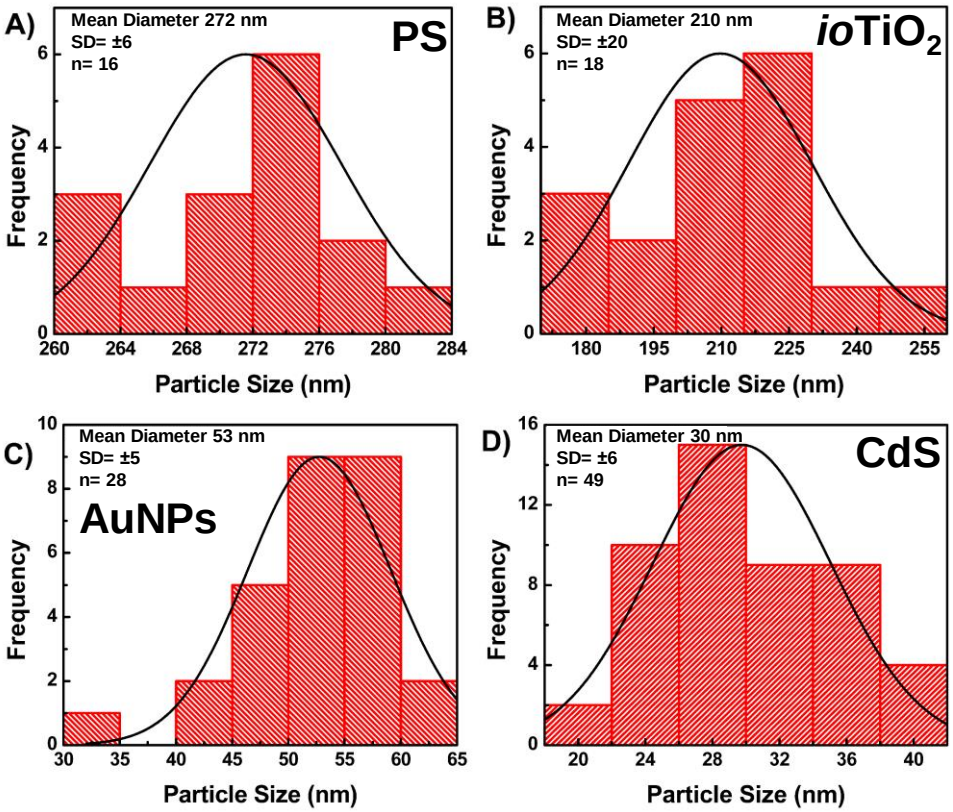

FIGURE 3.6 Size distribution histograms for (A) polystyrene, (B) *io*TiO_2, (C) AuNPs, and (D) CdS QDs. Determined by sampling *n* number of particles with imageJ software.

Particle size distributions were measured with imageJ software by taking the average of *n* number of particles. Histograms are shown in Figure 3.6. The polystyrene nanospheres were determined to be 272 ±6 nm in diameter. The TiO_2 inverse opals exhibited a size contraction of 22.8% to 210 ±20 nm which is within expectations.[36,37] AuNPs and CdS QDs were measured at 53 ±5 nm and 30 ±6 nm respectively.

Elemental components were confirmed with EDX (Figure 3.7). The medium and small peaks at 4.49 and 4.9 keV respectively are indicative of titanium emitted Kα and Lα X-rays. Consequently, these peaks are featured in all spectra except for the CdS thin film (blue), thereby demonstrating the presence of titanium. The sharp peak at 0.53 keV is

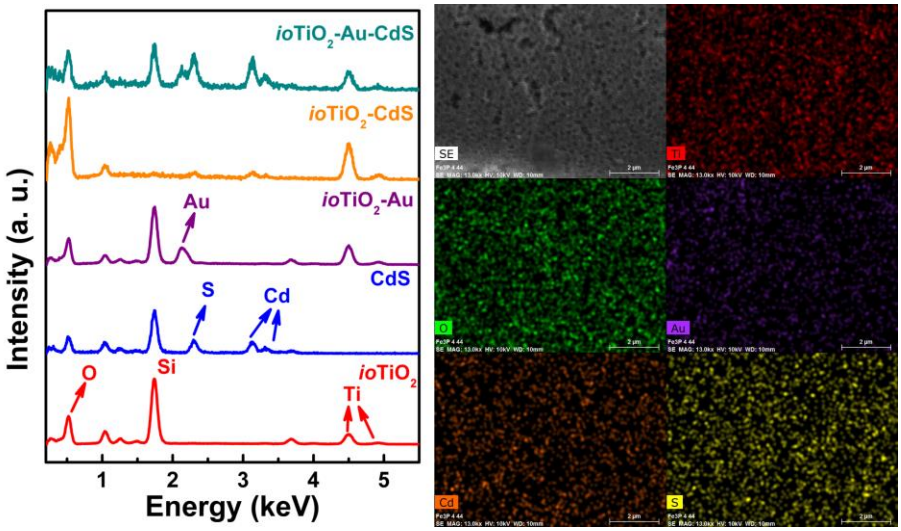

FIGURE 3.7 EDX spectra for photocatalytic systems *io*TiO_2 (red), CdS (blue), *io*TiO_2-Au (purple), *io*TiO_2CdS (orange), and *io*TiO_2-Au-CdS (green) (left) and EDX elemental component mapping for the *io*TiO_2-Au-CdS ternary system (right)

characteristic to oxygen Kα emission and is present in all the spectra. This is sensible for the TiO_2 containing slides, however, its presence in the CdS spectra can be ascribed to the glass substrate containing SiO_2. Accordingly, the very sharp peak at 1.74 keV denotes the Kα emission of silicon. The cadmium peaks are most prominent at 3.14 and 3.32 keV (Lα), and the corresponding sulfur peak can be seen at 2.30 keV (Kα). These peaks are only present in the CdS containing slides, CdS thin film, *io*TiO_2-CdS (orange), and *io*TiO_2-Au-CdS (green). Finally, only the 2.13 keV M series gold peak is visible and is present in the *io*TiO_2-Au (purple) and *io*TiO_2-Au-CdS spectra. The 9.71 keV Lα peak was not observed with 10 keV accelerating voltage. The peaks at 0.277, 1.04, and 1.254 keV are typical of Kα emissions from carbon, sodium, and magnesium, which are likely attributed to combustion residue from

TABLE 3.1 Normalized weight and atomic percentage for *io*TiO_2-Au-CdS ternary system components

Element	Series	Energy (keV)	Normalized Weight %	Normalized Atomic %
Oxygen	K-series	0.53	30.29	61.12
Titanium	K-series	4.49	41.21	27.78
Sulfur	K-series	2.30	5.05	5.09
Cadmium	L-series	3.14	17.62	5.06
Gold	M-series	2.13	5.83	0.96

the polymer (for carbon) or the glass substrate (Na and Mg). The accompanying EDX mapping images show even distribution of the elemental components Ti, O, Au, Cd, and S. Normalized atomic percentages (Table 3.1) fall within expected ratios. Oxygen (61.12%) and titanium (27.78%) are in a ~2:1 ratio, cadmium (5.06%) and sulfur (5.09%) are almost exactly 1:1, and gold made up the smallest percentage at 0.96%.

3.4 Thin Film UV-visible Absorbance Analysis

Normalized solid-state spectra of the films were taken to illustrate shifts in the thin films' visible absorbance (Figure 3.8). Plain *io*TiO_2 (red) primarily absorbs around 400 nm and below due to its wide band gap.[80] The CdS thin film's absorbance (blue) jumps at around 500 nm which corresponds closely to its narrower band gap of 2.4 eV.[81] Binary *io*TiO_2-Au (purple) has a broader shoulder that reaches to roughly 550 nm due to the LSPR effect generated by the AuNPs, which can vary with nanoparticle size and shape.[82] The binary *io*TiO_2-CdS (orange) system also shows broadening to ~520 nm signifying

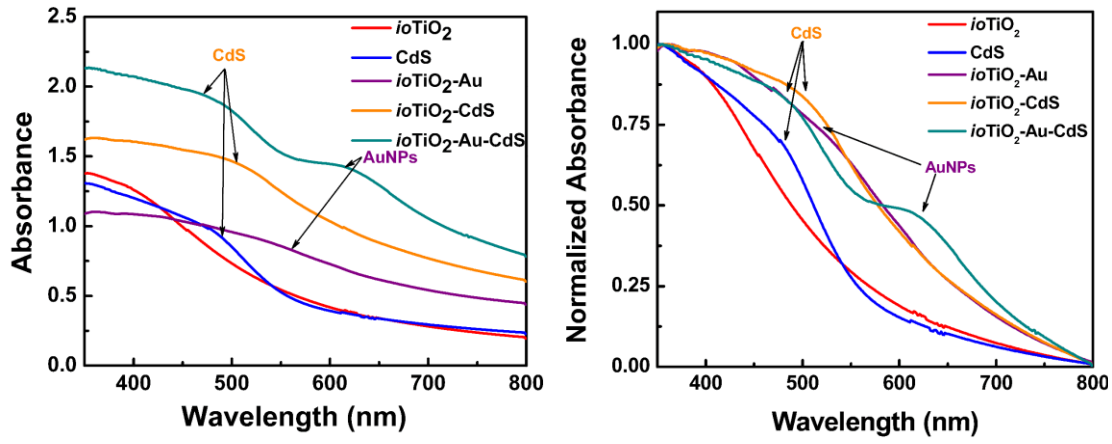

FIGURE 3.8 Solid-state absorbance spectra for photocatalyst thin films, (left) absolute optical absorbance and (right) normalized optical absorbance for *io*TiO_2 (red), CdS (blue), *io*TiO_2-Au (purple), *io*TiO_2CdS (orange), and *io*TiO_2-Au-CdS (green) thin films.

sensitization.[81] Likewise, the ternary *io*TiO_2-Au-CdS (green) shows broadening, however interestingly a second peak appears at 650 nm that is not present in either of the binary systems. This peak only occurs when both Au and CdS are present, and is possibly an indication of strong electromagnetic coupling red-shifting the LSPR band.[83,84]

3.5 Raman Spectroscopic Characterization

Raman spectra for the composites are displayed in Figure 3.9 below. The spectrum for *io*TiO_2 (red) contains one major peak at 150 cm^{-1} and three small peaks at 394, 514, and 639 cm^{-1} corresponding to the, B_{1g}, B_{1g}+A_{1g}, and E_g modes of vibration characteristic to the anatase TiO_2 polymorph.[85,86] The absence of signals at 234, 447, and 612 cm^{-1} for the B_{1g}, E_g, and A_{1g} modes of rutile indicate no rutile phase was detected. The same peaks are present in *io*TiO_2-Au (purple) *io*TiO_2-CdS (orange), and *io*TiO_2-Au-CdS (green), confirming pure anatase in all of them. CdS (blue) possesses typical peaks at 306 and 603

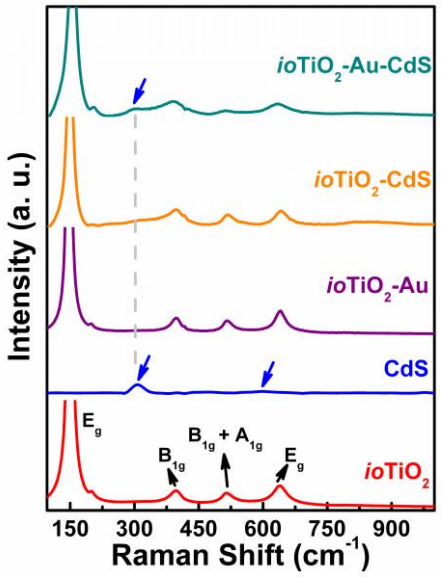

FIGURE 3.9 Thin film Raman spectra for *io*TiO_2 (red), CdS (blue), *io*TiO_2-Au (purple), *io*TiO_2CdS (orange), and *io*TiO_2-Au-CdS (green)

cm^{-1}.[85,87] Cadmium sulfide's 306 cm^{-1} peak is visible as a shoulder to the 394 cm^{-1} peak for titania in the *io*TiO_2-CdS, and *io*TiO_2-Au-CdS spectra, however the 603 cm^{-1} peak is not observable, and appears to have been overlapped with titania's 639 cm^{-1} peak. AuNPs are not Raman active, and thus the *io*TiO_2-Au spectrum is identical to plain *io*TiO_2 and *io*TiO_2-Au-CdS is identical to *io*TiO_2-CdS.

CHAPTER 4. PHOTOCATALYTIC DEGRADATION OF TRYPAN BLUE

4.1 Reactions Under Ultraviolet Light

The results for the photocatalytic degradation of trypan blue under UV light are depicted in Figure 4.1. As expected, all photocatalytic systems showed activity under UV light, however, the binary *io*TiO_2-CdS system (Figure 4.1E) was the only to reach completion after 180 minutes. Ternary *io*TiO_2-Au-CdS (Figure 4.1F) performed second best, achieving ~80% degradation in the same timeframe, while binary *io*TiO_2-Au (Figure 4.1D) performed very similarly to plain *io*TiO_2 (Figure 4.1B). There was a problem, however, with the CdS containing photocatalysts that is best typified in the case of the unary CdS thin film(Figure 4.1C), which is that of photocorrosion of the catalyst.[44,81,88,89] As can be seen, the first 30 minutes under irradiation exhibit relatively high photocatalytic

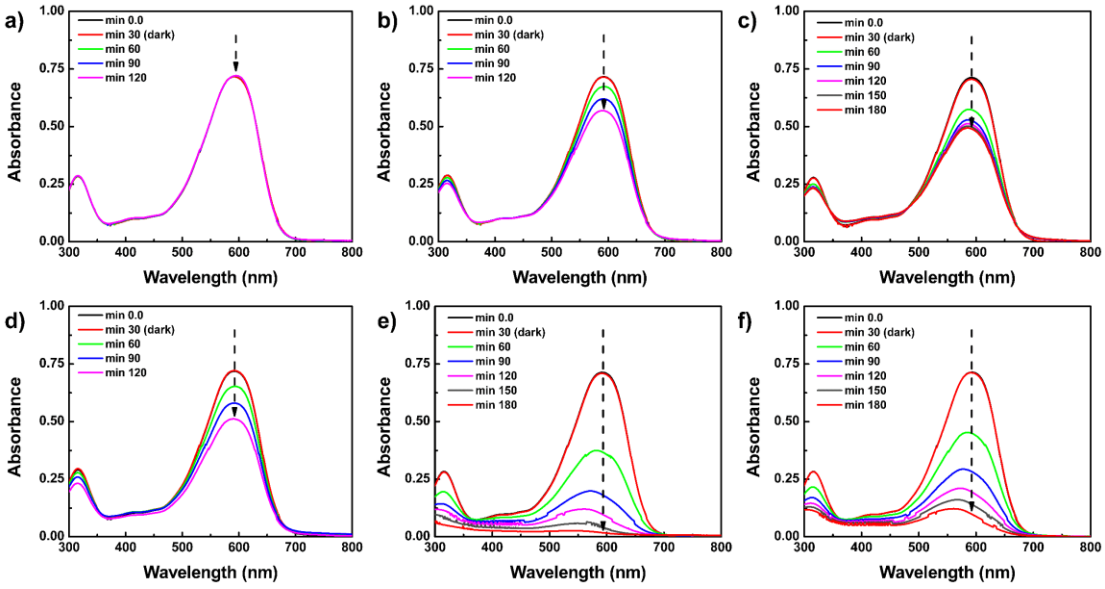

FIGURE 4.1 Absorption spectra of 20 µM TryB degradation under UV light for (A) a blank, (B) *io*TiO_2, (C) CdS thin film, (D) *io*TiO_2-Au, (E) *io*TiO_2-CdS, and (F) *io*TiO_2-Au-CdS

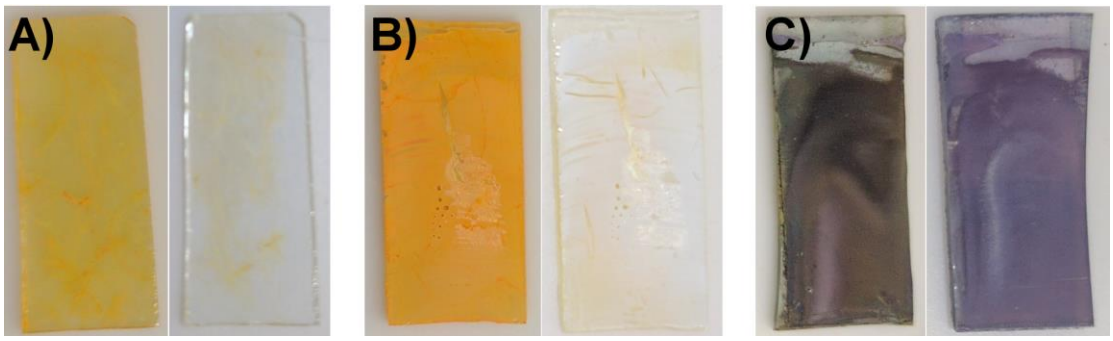

FIGURE 4.2 Photocatalytic thin film digital images pre- and post-reaction for (A) CdS, (B) *io*TiO_2-CdS, and (C) *io*TiO_2-Au-CdS showing loss of CdS due to photocorrosion.

activity, however this performance decreased with each succeeding measurement until activity ceased to be significant. The cause for this appears to be corrosion of CdS due to oxidation of S^{2-} into elemental sulfur or sulfur oxides,[90] and can be visualized by observing the gradual loss of the distinctive orange/yellow coloration of CdS over the course of the reaction (Figure 4.2A). Photocorrosion is also apparent in the *io*TiO_2-CdS (Figure 4.2B) and *io*TiO_2-Au-CdS (Figure 4.2C) reactions, however due to the greater stability of titania and gold the reactions could continue despite loss of CdS. Interestingly the ternary system did not return to the same purple coloration as the binary *io*TiO_2-Au system, but instead became more of a blue-purple color which further suggests strong interaction between the AuNPs and cadmium or sulfur.

Reaction kinetics can be seen in Figure 4.3. The requirement for light is demonstrated by the absence of activity in the first 30 minutes where the cuvettes are left in dark. It is only when the films are exposed to irradiation that TryB degradation occurs. It should also be noted that there appears to be no significant adsorption of the dye onto the thin films in this time-frame, indicating that the drop in TryB's UV-visible signal is entirely due to photocatalysis. Under UV lighting conditions the reactions appear to follow

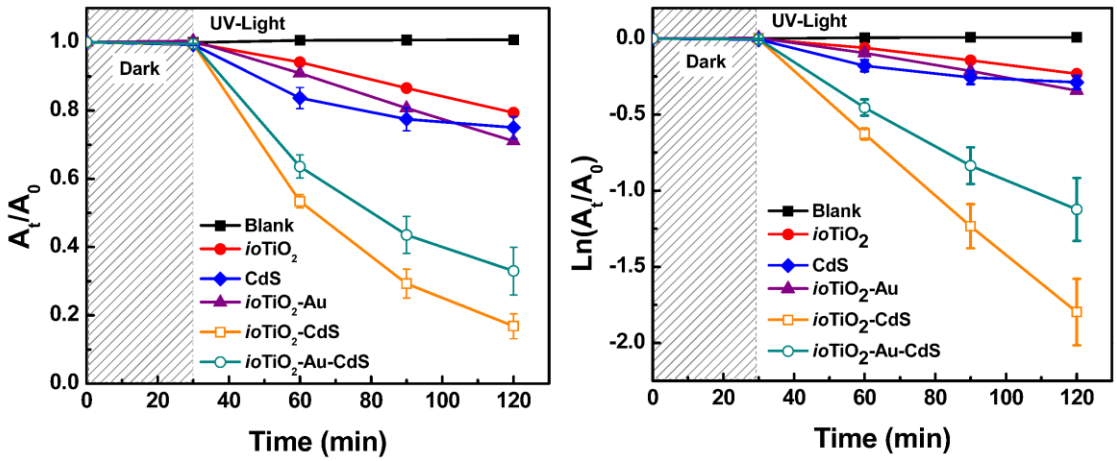

FIGURE 4.3 Reaction kinetics for UV degradation of 20 µM TryB (left) zero order and (right) psuedo first order for a blank (black), *io*TiO_2 (red), CdS (blue), *io*TiO_2-Au (purple), *io*TiO_2-CdS (orange), and *io*TiO_2-Au-CdS (green), taken at λ_{max} = 594 nm

the Langmuir-Hinshelwood first order model.[91] The rate constant (*k*) can thus be determined using Equation 2 where time (*t*) is in minutes:

$$\ln \frac{A_t}{A_0} = -kt \qquad \text{Eq. 2}$$

The resulting *k* constants and accompanying R^2 values are listed in Table 4.1. The binary *io*TiO_2-CdS showed the highest rate for TryB degradation at 0.01995 min^{-1}, which was 7.8, 5.2, 6.5, and 1.6 times faster than unary *io*TiO_2 (0.00257 min^{-1}) and CdS (0.00307 min^{-1}), binary *io*TiO_2-Au (0.00384 min^{-1}), and ternary *io*TiO_2-Au-CdS (0.01246 min^{-1}) respectively.

TABLE 4.1. Coefficients of determination and rate constants for pseudo first order TryB degradation under UV light

	R^2 (A_t/A_0)	R^2 (Ln A_t/A_0)	k_{UV} (min^{-1})
ioTiO_2	0.9965	0.9925	0.00257
CdS	0.8751	0.8955	0.00307
ioTiO_2-Au	0.9998	0.9969	0.00384
ioTiO_2-CdS	0.9278	0.9994	0.01995
ioTiO_2-Au-CdS	0.9367	0.9907	0.01246

Overall, TiO_2/CdS coupled systems significantly outperformed unary systems and *io*TiO_2-Au, however it is interesting to note the improved performance of binary *io*TiO_2-CdS over ternary *io*TiO_2-Au-CdS. Competition between sensitization and active site availability may play a role in the ternary system's reduced activity, since high AuNPs loading may block active sites and inhibit reactive oxygen species formation resulting in slower degradation rates.[92]

4.2 Reactions Under Visible LED

TryB degradation under visible LED can be seen in Figure 4.4. As with UV, binary *io*TiO_2-CdS (Figure 4.4E) and ternary *io*TiO_2-Au-CdS (Figure 4.4F) performed best, achieving about 55% and 60% degradation respectively after 120 minutes, however, the difference between the two was not statistically significant. Unary *io*TiO_2 (Figure 4.4B) and binary *io*TiO_2-Au (Figure 4.4D) showed very little activity due to titania's poor

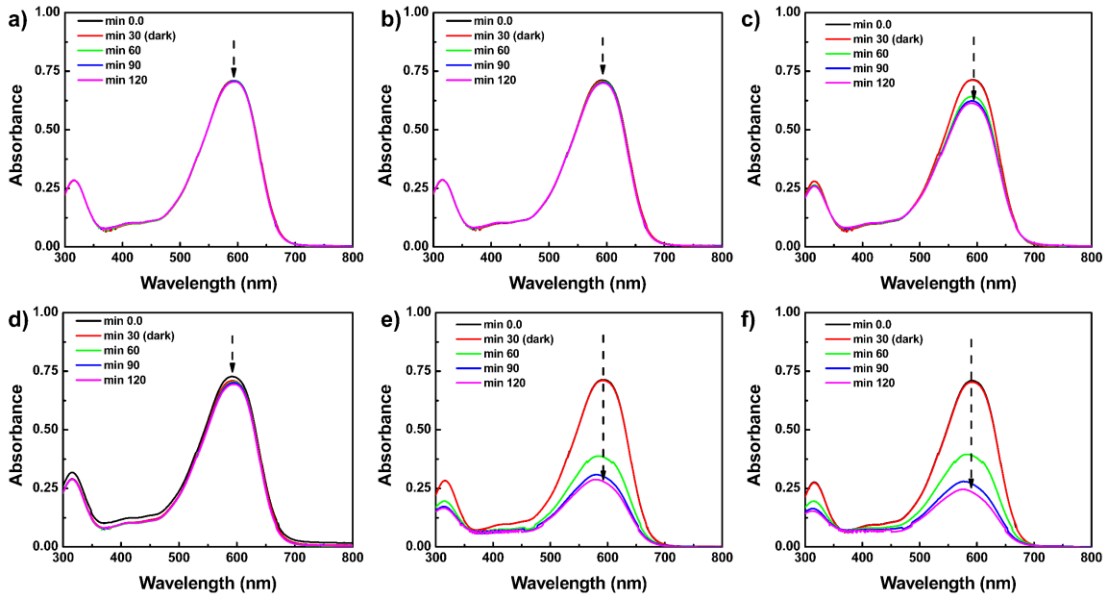

FIGURE 4.4 Absorption spectra of 20 µM TryB degradation under visible LED light for (A) a blank, (B) *io*TiO_2, (C) CdS thin film, (D) *io*TiO_2-Au, (E) *io*TiO_2-CdS, and (F) *io*TiO_2-Au-CdS

response under visible light, however *io*TiO_2-Au did show slight improvement suggesting possible sensitization. The CdS thin film (Figure 4.4C) still underwent photocorrosion as can be seen in its gradually slowing rate of TryB degradation, a feature which is also visible in the other CdS containing binary and ternary systems. Titania's lack of activity under visible light and the loss of CdS account for why neither *io*TiO_2-CdS nor *io*TiO_2-Au-CdS reached completion.

Reaction kinetics are illustrated in Figure 4.5. In general, TiO_2/CdS coupled systems outperformed unary systems and *io*TiO_2-Au, however the difference between *io*TiO_2-CdS and *io*TiO_2-Au-CdS was not significant. None of the CdS containing systems appear to follow zero or first order models so rate constants were not calculated.

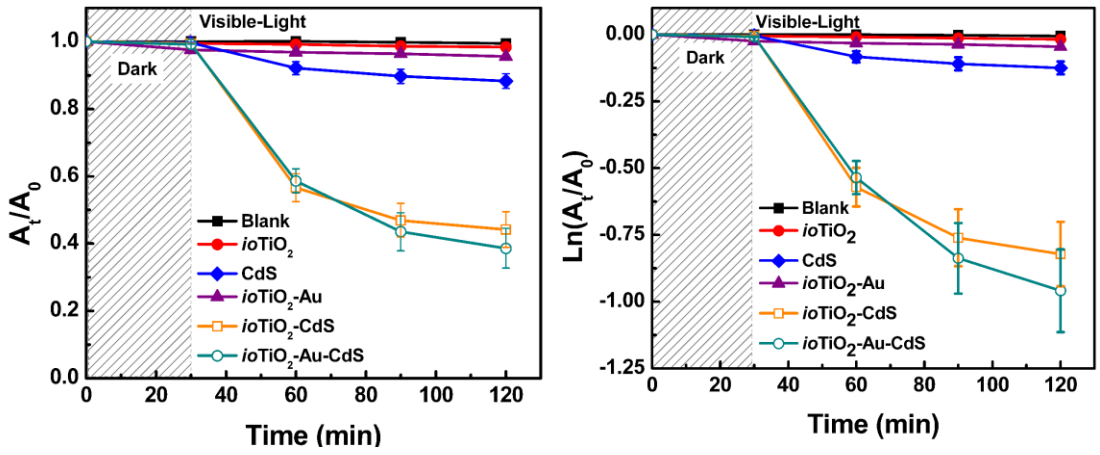

FIGURE 4.5 Reaction kinetics for Visible LED degradation of 20 µM TryB (left) zero order and (right) psuedo first order for a blank (black), *io*TiO_2 (red), CdS (blue), *io*TiO_2-Au (purple), *io*TiO_2-CdS (orange), and *io*TiO_2-Au-CdS (green), taken at λ_{max} = 594 nm

4.3 *Binary and Ternary Synergistic Effect*

To demonstrate the synergistic effect of incorporating the photosensitizers into binary and ternary systems, percent degradation of the dyes was compared. Percent degradation was defined per Equation 3:

$$\%\ Degradation = \left(1 - \frac{A_t}{A_0}\right) \times 100\% \qquad \text{Eq. 3}$$

Percent degradation for the two unary systems, *io*TiO_2 and CdS, and binary *io*TiO_2-Au plus CdS were summed together and plotted in Figure 4.6 along with percent degradation for the binary *io*TiO_2-CdS and ternary *io*TiO_2-Au-CdS composites. What is notable is the rate of dye degradation for both the binary *io*TiO_2-CdS and ternary *io*TiO_2-Au-CdS systems exceed the rate of degradation for their constituent parts summed together. This demonstrates that improved photocatalytic performance due to incorporation of photosensitizers into binary and ternary systems is more than simply a result of both sensitizers working simultaneously but independently. Coupling the photocatalysts

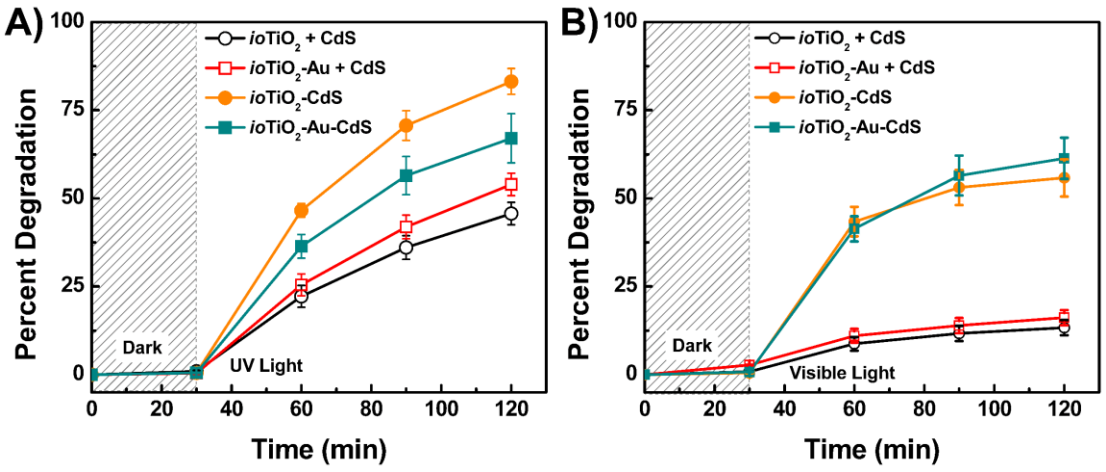

FIGURE 4.6 Synergistic effect for binary and ternary photocatalysts under UV (left) and visible LED (right) irradiation. The binary *io*TiO_2-CdS (orange) and ternary *io*TiO_2-Au-CdS (green) show higher activity than the sum of their constituent parts *io*TiO_2 + CdS (black) and *io*TiO_2-Au + CdS (red).

together results in a synergistic enhancement of activity which is likely attributed to factors such as improved electron-hole separation,[26] enhanced light harvesting ability,[20,42-44] increased surface area,[56] and better quantum dot distribution along the inverse opal structure.[17] Additionally, it is interesting to note that although the ternary system performed worse than or equal to the binary *io*TiO_2-CdS system, it performed the most consistently across both light sources, attaining 67% and 61% degradation in 120 minutes under UV and visible conditions (92% activity retention). By contrast binary *io*TiO_2-CdS dropped from 83% to 56% (67% activity retention) and unary CdS from 25% to 12% (48% activity retention). Binary *io*TiO_2-Au and unary *io*TiO_2 retained 15% and 8% of their UV activity respectively.

4.4 Proposed Mechanism of Degradation

TiO_2 photocatalysis is classified as an AOP, thus a possible degradation mechanism for the ternary system is illustrated in Figure 4.7. Under visible light, an electron is excited from VB_{CdS} to CB_{CdS} generating a hole.[90,93] The photoexcited electron travels to CB_{TiO2} via the conductive AuNPs where it reacts with dissolved oxygen to form reactive oxygen species such as superoxide and hydroxyl radicals. The superoxides progress through a series of reactions with water to form more hydroxyl radicals which proceed to degrade

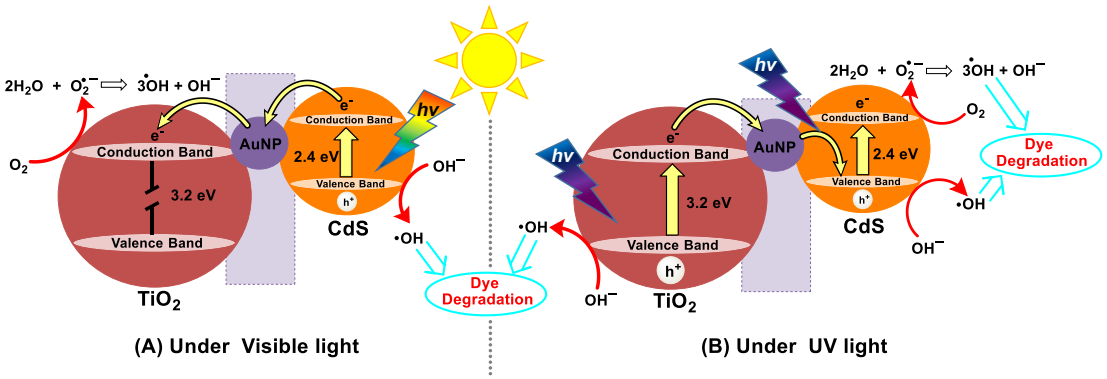

FIGURE 4.7 Proposed mechanism for TryB degradation for ternary *io*TiO_2-Au-CdS system under (A) visible and (B) UV irradiation

pollutants due to their strong reducing power.[9,22-24] Hydroxide ions formed in this process replenish the hole in the VB of CdS allowing the reaction to proceed anew. The reaction steps are outlined as follows:

$$CdS + h\upsilon\ (visible) \rightarrow CdS\ (e^- + h^+) \quad (1)$$

$$TiO_2 + h\upsilon\ (UV) \rightarrow TiO_2\ (e^- + h^+) \quad (2)$$

$$e^- + O_2 \rightarrow O_2^{\bullet -} \quad (3)$$

$$O_2^{\bullet -} + H_2O \rightarrow HO_2^{\bullet} + OH^- \quad (4)$$

$$HO_2^{\bullet} + H_2O \rightarrow H_2O_2 + OH^{\bullet} \quad (5)$$

$$H_2O_2 \rightarrow 2OH^{\bullet} \quad (6)$$

$$h^+ + OH^- \rightarrow OH^{\bullet} \quad (7)$$

$$OH^{\bullet} + TryB \rightarrow \text{Degradation products} \quad (8)$$

Under UV light titania becomes active, allowing for the pathway illustrated in Figure 4.7B. Here, an electron in VB_{TiO2} is excited CB_{TiO2} and transferred via AuNPs to VB_{CdS} where it undergoes excitation again to the CB_{CdS}. From here the electron is used to initiate a similar

series of reactions as above.[94] Improved electron-hole separation may contribute to the enhanced photocatalytic activity of the ternary system over unary and binary *io*TiO_2-Au, and the larger potential difference exhibited by the $VB_{TiO2} \rightarrow CB_{CdS}$ pathway vs the $VB_{CdS} \rightarrow CB_{TiO2}$ pathway likely explains the photocatalyst's greater performance under UV than visible LED.

Binary *io*TiO_2-CdS follows a similar mechanism as the ternary system, minus the AuNPs acting as a mediator, illustrated in Figure 4.8. Under visible light (Figure 4.8A) the binary Z-scheme system performs similarly to the ternary Z-scheme, however under UV light (Figure 4.8B) *io*TiO_2-CdS is much improved, suggesting the AuNPs are impeding the mechanism in some way. Further investigation is required to evaluate the AuNPs influence as a mediator on photocatalytic performance of the ternary system.

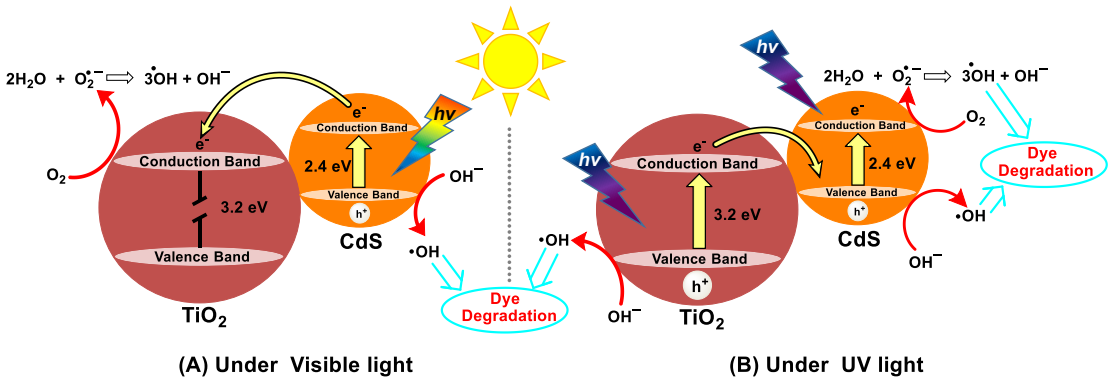

FIGURE 4.8 Proposed mechanism for TryB degradation for binary *io*TiO_2-CdS system under (A) visible and (B) UV irradiation

CONCLUSION

Unary, binary, and ternary inverse opal photocatalytic systems were successfully fabricated. The materials, labeled *io*TiO_2, CdS, *io*TiO_2-Au, *io*TiO_2-CdS, and *io*TiO_2-Au-CdS, were characterized by SEM, EDX, solid state UV-visible, and Raman spectroscopies. Incorporating the components into binary and ternary composites based on an inverse opal foundation improves their light harvesting capabilities, and as a result, their photocatalytic performance have been enhanced. Reaction kinetics for the photocatalysts were determined to be a pseudo first order reactions under UV light, and it was found that dual semiconductor based 'Z-Scheme' systems demonstrated superior photocatalytic activity for degradation of TryB over pure sensitization with AuNPs under both visible LED and UV lighting conditions. Indeed, the binary *io*TiO_2-CdS performed better than (under UV) or at the same level (under visible) as ternary *io*TiO_2-Au-CdS, however, the ternary system performed more consistently across the different irradiation sources, retaining 92% of it UV degradation activity under visible LED compared to 67% activity retention in the *io*TiO_2-CdS system. Despite this, it was found that all CdS incorporating systems underwent photocorrosion due to possible oxidation of S^{2-} ions to elemental sulfur and sulfur oxides. Loss of the CdS QDs resulted in a significant reduction in activity over time and severely limits recyclability of the photocatalyst. Further investigation is required into the influence AuNPs have on photocatalytic performance and to find a way to stabilize CdS to mitigate its corrosion.

REFERENCES

1. Konstantinou, I. K.; Albanis, T. A. TiO 2-assisted photocatalytic degradation of azo dyes in aqueous solution: kinetic and mechanistic investigations: a review. *Appl. Catal., B* **2004**, *49*, 1-14.

2. Cheng, H.; Wang, J.; Zhao, Y.; Han, X. Effect of phase composition, morphology, and specific surface area on the photocatalytic activity of TiO 2 nanomaterials. *RSC Adv.* **2014**, *4*, 47031-47038.

3. Castellote, M.; Bengtsson, N. Principles of TiO2 photocatalysis. In *Applications of Titanium Dioxide Photocatalysis to Construction Materials*Springer: 2011; pp 5-10.

4. Maeda, K. Z-scheme water splitting using two different semiconductor photocatalysts. *ACS Catal.* **2013**, *3*, 1486-1503.

5. Park, N.; Van de Lagemaat, J.; Frank, A. J. Comparison of dye-sensitized rutile-and anatase-based TiO2 solar cells. *J. Phys. Chem. B* **2000**, *104*, 8989-8994.

6. Lai, Y.; Tang, Y.; Gong, J.; Gong, D.; Chi, L.; Lin, C.; Chen, Z. Transparent superhydrophobic/superhydrophilic TiO 2-based coatings for self-cleaning and anti-fogging. *J. Mater. Chem. A* **2012**, *22*, 7420-7426.

7. Watanabe, T.; Nakajima, A.; Wang, R.; Minabe, M.; Koizumi, S.; Fujishima, A.; Hashimoto, K. Photocatalytic activity and photoinduced hydrophilicity of titanium dioxide coated glass. *Thin Solid Films* **1999**, *351*, 260-263.

8. Verma, A.; Prakash, N. T.; Toor, A. P. An efficient TiO2 coated immobilized system for the degradation studies of herbicide isoproturon: durability studies. *Chemosphere* **2014**, *109*, 7-13.

9. Daghrir, R.; Drogui, P.; Robert, D. Modified TiO2 for environmental photocatalytic applications: a review. *Ind Eng Chem Res* **2013**, *52*, 3581-3599.

10. Momma, K.; Izumi, F. VESTA 3 for three-dimensional visualization of crystal, volumetric and morphology data. *J. Appl. Crystallogr.* **2011**, *44*, 1272-1276.

11. Howard, C. J.; Sabine, T. M.; Dickson, F. Structural and thermal parameters for rutile and anatase. *Acta Crystallogr. Sect. B* **1991**, *47*, 462-468.

12. Gonschorek, W.; Feld, R. Neutron diffraction study. *Z Kristallogr* **1982**, *161*, 1-5.

13. Liu, L.; Zhao, H.; Andino, J. M.; Li, Y. Photocatalytic CO2 reduction with H2O on TiO2 nanocrystals: Comparison of anatase, rutile, and brookite polymorphs and exploration of surface chemistry. *ACS Catal.* **2012**, *2*, 1817-1828.

14. Ding, Z.; Lu, G. Q.; Greenfield, P. F. Role of the crystallite phase of TiO2 in heterogeneous photocatalysis for phenol oxidation in water. *J. Phys. Chem. B* **2000**, *104*, 4815-4820.

15. Luttrell, T.; Halpegamage, S.; Tao, J.; Kramer, A.; Sutter, E.; Batzill, M. Why is anatase a better photocatalyst than rutile?-Model studies on epitaxial TiO2 films. *Sci. Rep.* **2014**, *4*, 4043.

16. Cappelletti, G.; Bianchi, C. L.; Ardizzone, S. Nano-titania assisted photoreduction of Cr (VI): the role of the different TiO2 polymorphs. *Appl. Catal., B* **2008**, *78*, 193-201.

17. Cheng, C.; Karuturi, S. K.; Liu, L.; Liu, J.; Li, H.; Su, L. T.; Tok, A. I. Y.; Fan, H. J. Quantum-Dot-Sensitized TiO2 Inverse Opals for Photoelectrochemical Hydrogen Generation. *Small* **2012**, *8*, 37-42.

18. Gonzlez, S.; Fernndez-Lorente, M.; Gilaberte-Calzada, Y. The latest on skin photoprotection. *Clin. Dermatol.* **2008**, *26*, 614-626.

19. Bais, A. F.; McKenzie, R. L.; Bernhard, G.; Aucamp, P. J.; Ilyas, M.; Madronich, S.; Tourpali, K. Ozone depletion and climate change: impacts on UV radiation. *Photochem. Photobiol. Sci.* **2015**, *14*, 19-52.

20. Wang, Y.; Xiong, D.; Zhang, W.; Su, H.; Liu, Q.; Gu, J.; Zhu, S.; Zhang, D. Surface plasmon resonance of gold nanocrystals coupled with slow-photon-effect of biomorphic TiO 2 photonic crystals for enhanced photocatalysis under visible-light. *Catal. Today* **2016**, *274*, 15-21.

21. Kudo, A.; Miseki, Y. Heterogeneous photocatalyst materials for water splitting. *Chem. Soc. Rev.* **2009**, *38*, 253-278.

22. Stasinakis, A. S. Use of selected advanced oxidation processes (AOPs) for wastewater treatment—a mini review. *Global NEST J* **2008**, *10*, 376-385.

23. Yu, Z.; Chuang, S. S. The effect of Pt on the photocatalytic degradation pathway of methylene blue over TiO 2 under ambient conditions. *Appl. Catal., B* **2008**, *83*, 277-285.

24. Mahvi, A. H.; Ghanbarian, M.; Nasseri, S.; Khairi, A. Mineralization and discoloration of textile wastewater by TiO2 nanoparticles. *Desalination* **2009**, *239*, 309-316.

25. Chen, X.; Shen, S.; Guo, L.; Mao, S. S. Semiconductor-based photocatalytic hydrogen generation. *Chem. Rev.* **2010**, *110*, 6503.

26. Zhou, P.; Yu, J.; Jaroniec, M. All-Solid-State Z-Scheme Photocatalytic Systems. *Adv Mater* **2014**, *26*, 4920-4935.

27. Xia, L.; Xu, L.; Song, J.; Xu, R.; Liu, D.; Dong, B.; Song, H. CdS quantum dots modified CuO inverse opal electrodes for ultrasensitive electrochemical and photoelectrochemical biosensor. *Sci. Rep.* **2015**, *5*, 10838.

28. Li, Y.; Piret, F.; Léonard, T.; Su, B. Rutile TiO 2 inverse opal with photonic bandgap in the UV–visible range. *J. Colloid Interface Sci.* **2010**, *348*, 43-48.

29. Ibhadon, A. O.; Fitzpatrick, P. Heterogeneous photocatalysis: recent advances and applications. *Catalysts* **2013**, *3*, 189-218.

30. Curti, M.; Schneider, J.; Bahnemann, D. W.; Mendive, C. B. Inverse opal photonic crystals as a strategy to improve photocatalysis: underexplored questions. *J. Phys. Chem. Lett.* **2015**, *6*, 3903-3910.

31. Chen, J. I.; von Freymann, G.; Choi, S. Y.; Kitaev, V.; Ozin, G. A. Amplified photochemistry with slow photons. *Adv Mater* **2006**, *18*, 1915-1919.

32. Johnson, S. G.; Joannopoulos, J. D. Introduction to photonic crystals: Bloch's theorem, band diagrams, and gaps (but no defects). *Photonic Crystal Tutorial* **2003**, 1-16.

33. Wu, M.; Jin, J.; Liu, J.; Deng, Z.; Li, Y.; Deparis, O.; Su, B. High photocatalytic activity enhancement of titania inverse opal films by slow photon effect induced strong light absorption. *J. Mater. Chem. A* **2013**, *1*, 15491-15500.

34. Chen, S.; Wang, A.; Dai, C.; Benziger, J. B.; Liu, X. The effect of photonic band gap on the photo-catalytic activity of nc-TiO 2/SnO 2 photonic crystal composite membranes. *Chem. Eng. J.* **2014**, *249*, 48-53.

35. Stein, A.; Schroden, R. C. Colloidal crystal templating of three-dimensionally ordered macroporous solids: materials for photonics and beyond. *Curr. Opin. Solid State Mater. Sci.* **2001**, *5*, 553-564.

36. Kwak, E. S.; Lee, W.; Park, N.; Kim, J.; Lee, H. Compact Inverse-Opal Electrode Using Non-Aggregated TiO2 Nanoparticles for Dye-Sensitized Solar Cells. *Adv. Funct. Mater.* **2009**, *19*, 1093-1099.

37. Hu, Z.; Xu, L.; Wang, L.; Huang, Y.; Xu, L.; Chen, J. One-step fabrication of N-doped TiO 2 inverse opal films with visible light photocatalytic activity. *Catal. Commun.* **2013**, *40*, 106-110.

38. Eustis, S.; El-Sayed, M. A. Why gold nanoparticles are more precious than pretty gold: noble metal surface plasmon resonance and its enhancement of the radiative and nonradiative properties of nanocrystals of different shapes. *Chem. Soc. Rev.* **2006**, *35*, 209-217.

39. Li, J.; Cushing, S. K.; Zheng, P.; Senty, T.; Meng, F.; Bristow, A. D.; Manivannan, A.; Wu, N. Solar hydrogen generation by a CdS-Au-TiO2 sandwich nanorod array enhanced with

Au nanoparticle as electron relay and plasmonic photosensitizer. *J. Am. Chem. Soc.* **2014**, *136*, 8438-8449.

40. Lu, Y.; Yu, H.; Chen, S.; Quan, X.; Zhao, H. Integrating plasmonic nanoparticles with TiO2 photonic crystal for enhancement of visible-light-driven photocatalysis. *Environ. Sci. Technol.* **2012**, *46*, 1724-1730.

41. Zhao, Y.; Yang, B.; Xu, J.; Fu, Z.; Wu, M.; Li, F. Facile synthesis of Ag nanoparticles supported on TiO 2 inverse opal with enhanced visible-light photocatalytic activity. *Thin Solid Films* **2012**, *520*, 3515-3522.

42. Robel, I.; Kuno, M.; Kamat, P. V. Size-dependent electron injection from excited CdSe quantum dots into TiO2 nanoparticles. *J. Am. Chem. Soc.* **2007**, *129*, 4136-4137.

43. Tisdale, W. A.; Williams, K. J.; Timp, B. A.; Norris, D. J.; Aydil, E. S.; Zhu, X. Hot-electron transfer from semiconductor nanocrystals. *Science* **2010**, *328*, 1543-1547.

44. Fujishima, M.; Nakabayashi, Y.; Takayama, K.; Kobayashi, H.; Tada, H. High coverage formation of CdS quantum dots on TiO2 by the photocatalytic growth of preformed seeds. *J. Phys. Chem. C* **2016**, *120*, 17365-17371.

45. Iwase, A.; Ng, Y. H.; Ishiguro, Y.; Kudo, A.; Amal, R. Reduced graphene oxide as a solid-state electron mediator in Z-scheme photocatalytic water splitting under visible light. *J. Am. Chem. Soc.* **2011**, *133*, 11054-11057.

46. Yun, J.; Ng, Y. H.; Huang, S.; Conibeer, G.; Amal, R. Wrapping the walls of n-TiO 2 nanotubes with p-CuInS 2 nanoparticles using pulsed-electrodeposition for improved heterojunction photoelectrodes. *Chem. Commun.* **2011**, *47*, 11288-11290.

47. Yang, L.; Luo, S.; Li, Y.; Xiao, Y.; Kang, Q.; Cai, Q. High efficient photocatalytic degradation of p-nitrophenol on a unique Cu2O/TiO2 pn heterojunction network catalyst. *Environ. Sci. Technol.* **2010**, *44*, 7641-7646.

48. Hou, Y.; Li, X.; Zhao, Q.; Quan, X.; Chen, G. Electrochemical method for synthesis of a ZnFe2O4/TiO2 composite nanotube array modified electrode with enhanced photoelectrochemical activity. *Adv. Funct. Mater.* **2010**, *20*, 2165-2174.

49. Pant, B.; Barakat, N. A.; Pant, H. R.; Park, M.; Saud, P. S.; Kim, J.; Kim, H. Synthesis and photocatalytic activities of CdS/TiO 2 nanoparticles supported on carbon nanofibers for high efficient adsorption and simultaneous decomposition of organic dyes. *J. Colloid Interface Sci.* **2014**, *434*, 159-166.

50. Yu, Z. B.; Xie, Y. P.; Liu, G.; Lu, G. Q. M.; Ma, X. L.; Cheng, H. Self-assembled CdS/Au/ZnO heterostructure induced by surface polar charges for efficient photocatalytic hydrogen evolution. *J. Mater. Chem. A* **2013**, *1*, 2773-2776.

51. Lin, H.; Cao, J.; Luo, B.; Xu, B.; Chen, S. Synthesis of novel Z-scheme AgI/Ag/AgBr composite with enhanced visible light photocatalytic activity. *Catal. Commun.* **2012**, *21*, 91-95.

52. Kim, H. G.; Jeong, E. D.; Borse, P. H.; Jeon, S.; Yong, K.; Lee, J. S.; Li, W.; Oh, S. H. Photocatalytic Ohmic layered nanocomposite for efficient utilization of visible light photons. *Appl. Phys. Lett.* **2006**, *89*, 064103.

53. Yun, D.; Lee, H.; Jang, H.; Yoo, J. Controlling size and distribution for nano-sized polystyrene spheres. *Bull. Korean Chem. Soc.* **2010**, *31*, 1345-1348.

54. Pyrz, W. D.; Buttrey, D. J. Particle size determination using TEM: a discussion of image acquisition and analysis for the novice microscopist. *Langmuir* **2008**, *24*, 11350-11360.

55. Woehrle, G. H.; Hutchison, J. E.; zkar, S.; FINKE, R. G. Analysis of nanoparticle transmission electron microscopy data using a public-domain image-processing program, image. *Turk J Chem* **2006**, *30*, 1-13.

56. Waterhouse, G. I.; Waterland, M. R. Opal and inverse opal photonic crystals: fabrication and characterization. *Polyhedron* **2007**, *26*, 356-368.

57. Kamegawa, T.; Suzuki, N.; Yamashita, H. Design of macroporous TiO 2 thin film photocatalysts with enhanced photofunctional properties. *Energy Environ Sci.* **2011**, *4*, 1411-1416.

58. Mishchenko, L.; Hatton, B.; Burgess, I. B.; Davis, S.; Sandhage, K.; Aizenberg, J. In *In Colloidal co-assembly route to large-area, high-quality photonic crystals;* Proc. of SPIE Vol; 2011; Vol. 7946, pp 1.

59. Scheid, D.; Stock, D.; Winter, T.; Gutmann, T.; Dietz, C.; Gallei, M. The pivotal step of nanoparticle functionalization for the preparation of functional and magnetic hybrid opal films. *J. Mater. Chem. C* **2016**, *4*, 2187-2196.

60. Hatton, B.; Mishchenko, L.; Davis, S.; Sandhage, K. H.; Aizenberg, J. Assembly of large-area, highly ordered, crack-free inverse opal films. *Proc. Natl. Acad. Sci. U. S. A.* **2010**, *107*, 10354-10359.

61. Singh, M.; Haverinen, H. M.; Dhagat, P.; Jabbour, G. E. Inkjet printing—process and its applications. *Adv Mater* **2010**, *22*, 673-685.

62. Bankar, A.; Joshi, B.; Kumar, A. R.; Zinjarde, S. Banana peel extract mediated synthesis of gold nanoparticles. *Colloids Surf., B* **2010**, *80*, 45-50.

63. Sankapal, B. R.; Mane, R. S.; Lokhande, C. D. Deposition of CdS thin films by the successive ionic layer adsorption and reaction (SILAR) method. *Mater. Res. Bull.* **2000**, *35*, 177-184.

64. Lee, H.; Leventis, H. C.; Moon, S.; Chen, P.; Ito, S.; Haque, S. A.; Torres, T.; Nüesch, F.; Geiger, T.; Zakeeruddin, S. M. PbS and CdS Quantum Dot-Sensitized Solid-State Solar Cells:"Old Concepts, New Results". *Adv. Funct. Mater.* **2009**, *19*, 2735-2742.

65. Hartman, C. P.; Fulk, G. E.; Andrews, A. W. Azo reduction of trypan blue to a known carcinogen by a cell-free extract of a human intestinal anaerobe. *Mutat Res-Getet Tox* **1978**, *58*, 125-132.

66. de Lima, Rodrigo Otvio Alves; Bazo, A. P.; Salvadori, D. M. F.; Rech, C. M.; de Palma Oliveira, D.; de Arago Umbuzeiro, G. Mutagenic and carcinogenic potential of a textile azo dye processing plant effluent that impacts a drinking water source. *Mutat Res-Getet Tox En* **2007**, *626*, 53-60.

67. Rochkind, M.; Pasternak, S.; Paz, Y. Using dyes for evaluating photocatalytic properties: a critical review. *Molecules* **2014**, *20*, 88-110.

68. Abdel-Maksoud, Y.; Imam, E.; Ramadan, A. TiO2 Solar Photocatalytic Reactor Systems: Selection of Reactor Design for Scale-up and Commercialization—Analytical Review. *Catalysts* **2016**, *6*, 138.

69. Lei, L.; Wang, N.; Zhang, X. M.; Tai, Q.; Tsai, D. P.; Chan, H. L. Optofluidic planar reactors for photocatalytic water treatment using solar energy. *Biomicrofluidics* **2010**, *4*, 043004.

70. Padfield, J. Spectral Power Distribution (SPD) Curves. *http://research.ng-london.org.uk/scientific/spd/?page=home* (accessed March 7, 2017).

71. Repo, E.; Rengaraj, S.; Pulkka, S.; Castangnoli, E.; Suihkonen, S.; Sopanen, M.; Sillanp, M. Photocatalytic degradation of dyes by CdS microspheres under near UV and blue LED radiation. *Sep. Purif. Technol.* **2013**, *120*, 206-214.

72. Wang, X.; Tang, Y.; Chen, Z.; Lim, T. Highly stable heterostructured Ag–AgBr/TiO 2 composite: a bifunctional visible-light active photocatalyst for destruction of ibuprofen and bacteria. *J. Mater. Chem.* **2012**, *22*, 23149-23158.

73. Perkampus, H.; Grinter, H.; Threlfall, T. L. *UV-VIS Spectroscopy and its Applications;* Springer: 1992; .

74. Sugioka, M. The Relationship Between UV-VIS Absorption and Structure of Organic Compounds. *UV Talk Letter February.Shimadzu* **2009**, *2*, 5-6.

75. Hunger, M.; Weitkamp, J. In situ IR, NMR, EPR, and UV/Vis spectroscopy: Tools for new insight into the mechanisms of heterogeneous catalysis. *Angew. Chem. Int. Ed.* **2001**, *40*, 2954-2971.

76. Haiss, W.; Thanh, N. T.; Aveyard, J.; Fernig, D. G. Determination of size and concentration of gold nanoparticles from UV− Vis spectra. *Anal. Chem.* **2007**, *79*, 4215-4221.

77. Larkin, P. *Infrared and Raman spectroscopy: principles and spectral interpretation;* Elsevier: 2011; .

78. Goldstein, J.; Newbury, D. E.; Echlin, P.; Joy, D. C.; Romig Jr, A. D.; Lyman, C. E.; Fiori, C.; Lifshin, E. *Scanning electron microscopy and X-ray microanalysis: a text for biologists, materials scientists, and geologists;* Springer Science & Business Media: 2012; .

79. Jiang, P.; Bertone, J. F.; Hwang, K. S.; Colvin, V. L. Single-crystal colloidal multilayers of controlled thickness. *Chem. Mater.* **1999**, *11*, 2132-2140.

80. Irie, H.; Watanabe, Y.; Hashimoto, K. Nitrogen-concentration dependence on photocatalytic activity of TiO2-x N x powders. *J. Phys. Chem. B* **2003**, *107*, 5483-5486.

81. Jang, J. S.; Ji, S. M.; Bae, S. W.; Son, H. C.; Lee, J. S. Optimization of CdS/TiO 2 nano-bulk composite photocatalysts for hydrogen production from Na 2 S/Na 2 SO 3 aqueous electrolyte solution under visible light ($\lambda \geq$ 420nm). *J. Photochem. Photobiol. A.* **2007**, *188*, 112-119.

82. Schmucker, A. L.; Harris, N.; Banholzer, M. J.; Blaber, M. G.; Osberg, K. D.; Schatz, G. C.; Mirkin, C. A. Correlating nanorod structure with experimentally measured and theoretically predicted surface plasmon resonance. *ACS Nano* **2010**, *4*, 5453-5463.

83. Zhao, H.; Wu, M.; Liu, J.; Deng, Z.; Li, Y.; Su, B. Synergistic promotion of solar-driven H 2 generation by three-dimensionally ordered macroporous structured TiO 2-Au-CdS ternary photocatalyst. *Appl. Catal., B* **2016**, *184*, 182-190.

84. Honma, I.; Sano, T.; Komiyama, H. Surface-enhanced Raman scattering (SERS) for semiconductor microcrystallites observed in Ag-CdS hybrid particles. *J. Phys. Chem.* **1993**, *97*, 6692-6695.

85. Kim, M.; Kim, Y. K.; Lim, S. K.; Kim, S.; In, S. Efficient visible light-induced H 2 production by Au@ CdS/TiO 2 nanofibers: Synergistic effect of core–shell structured Au@ CdS and densely packed TiO 2 nanoparticles. *Appl. Catal., B* **2015**, *166*, 423-431.

86. Liu, G.; Yang, H. G.; Sun, C.; Cheng, L.; Wang, L.; Lu, G. Q. M.; Cheng, H. Titania polymorphs derived from crystalline titanium diboride. *CrystEngComm* **2009**, *11*, 2677-2682.

87. Xian, J.; Li, D.; Chen, J.; Li, X.; He, M.; Shao, Y.; Yu, L.; Fang, J. TiO2 Nanotube Array—Graphene—CdS Quantum Dots Composite Film in Z-Scheme with Enhanced Photoactivity and Photostability. *ACS Appl. Mater. Interfaces* **2014**, *6*, 13157-13166.

88. Serpone, N.; Maruthamuthu, P.; Pichat, P.; Pelizzetti, E.; Hidaka, H. Exploiting the interparticle electron transfer process in the photocatalysed oxidation of phenol, 2-chlorophenol and pentachlorophenol: chemical evidence for electron and hole transfer between coupled semiconductors. *J. Photochem. Photobiol. A.* **1995**, *85*, 247-255.

89. Fujii, H.; Ohtaki, M.; Eguchi, K.; Arai, H. Preparation and photocatalytic activities of a semiconductor composite of CdS embedded in a TiO 2 gel as a stable oxide semiconducting matrix. *J. Mol. Catal. A: Chem.* **1998**, *129*, 61-68.

90. Tong, R.; Liu, C.; Xu, Z.; Kuang, Q.; Xie, Z.; Zheng, L. Efficiently Enhancing Visible Light Photocatalytic Activity of Faceted TiO2 Nanocrystals by Synergistic Effects of Core–Shell Structured Au@ CdS Nanoparticles and Their Selective Deposition. *ACS Appl. Mater. Interfaces* **2016**, *8*, 21326-21333.

91. Konstantinou, I. K.; Sakellarides, T. M.; Sakkas, V. A.; Albanis, T. A. Photocatalytic degradation of selected s-triazine herbicides and organophosphorus insecticides over aqueous TiO2 suspensions. *Environ. Sci. Technol.* **2001**, *35*, 398-405.

92. Murdoch, M.; Waterhouse, G.; Nadeem, M. A.; Metson, J. B.; Keane, M. A.; Howe, R. F.; Llorca, J.; Idriss, H. The effect of gold loading and particle size on photocatalytic hydrogen production from ethanol over Au/TiO2 nanoparticles. *Nat. Chem.* **2011**, *3*, 489.

93. Li, X.; Chen, X.; Niu, H.; Han, X.; Zhang, T.; Liu, J.; Lin, H.; Qu, F. The synthesis of CdS/TiO 2 hetero-nanofibers with enhanced visible photocatalytic activity. *J. Colloid Interface Sci.* **2015**, *452*, 89-97.

94. Arabzadeh, A.; Salimi, A. One dimensional CdS nanowire@ TiO 2 nanoparticles core-shell as high performance photocatalyst for fast degradation of dye pollutants under visible and sunlight irradiation. *J. Colloid Interface Sci.* **2016**, *479*, 43-54.